<u>GEORGIA DOT RESEARCH PROJECT 09-08</u>

FINAL REPORT

ESTIMATING FOUNDATION SCOUR FOR EXTREME HYDROLOGIC EVENTS AT SCOUR-CRITICAL BRIDGES

Georgia Department of Transportation

OFFICE OF RESEARCH
15 Kennedy Drive
Forest Park, GA 30297-2534

1.Report No.: FHWA-GA-RPXX	2. Government Accession No.:	3. Recipient's Catalog No.:

4. Title and Subtitle: Estimating Foundation Scour for Extreme Hydrologic Events at Scour-Critical Bridges	5. Report Date: February 2016
	6. Performing Organization Code:
7. Author(s): Terry W. Sturm, Thorsten Stoesser, Seungho Hong, Sibel Kara, and Yung-Chieh (Becky) Wang	8. Performing Organ. Report No.:
9. Performing Organization Name and Address: Georgia Institute of Technology School of Civil & Environmental Engineering 790 Atlantic Dr Atlanta, GA 30332-0355	10. Work Unit No.:
	11. Contract or Grant No.: XXXXXXXX
12. Sponsoring Agency Name and Address: Georgia Department of Transportation Office of Research 15 Kennedy Drive Forest Park, GA 30297-2534	13. Type of Report and Period Covered: Final; Feb. 2010 – March 2013
	14. Sponsoring Agency Code:

15. Supplementary Notes:
Prepared in cooperation with the U.S. Department of Transportation, Federal Highway Administration.

16. Abstract: During extreme hydrologic events, bridges may be subjected to submerged orifice flow and overtopping because they were not designed for such large flows. As a result, such bridges are vulnerable to excessive scour of the foundations and possible failure. The objective of this research is to examine both the hydrodynamics of the flow and the scour resistance of fine sediments to improve prediction of scour depths under extreme flooding conditions. The research approach is three-pronged: (1) experimental measurement of the scour depths and flow field in a large compound channel flume; (2) application of computational fluid dynamics to predict the turbulence properties of the flow field; and (3) testing of laboratory mixtures of fine sediments to develop a relationship for critical shear stress at the threshold of scour. Results of these three tasks are combined to form a procedure for scour prediction that considers both the causative and resistive factors in the complex process of bridge scour.

17. Key Words: bridge, sediment, scour, critical shear stress, computational fluid dynamics	18. Distribution Statement:

19. Security Classification (of this report): Unclassified	20. Security Classification (of this page): Unclassified	21. Number of Pages: 99	22. Price:

GDOT Research Project No. 09-08

Final Report

ESTIMATING FOUNDATION SCOUR FOR EXTREME HYDROLOGIC EVENTS AT SCOUR-CRITICAL BRIDGES

By

Terry W. Sturm, Thorsten Stoesser,
Seungho Hong, Sibel Kara, and Yung-Chieh (Becky) Wang

Georgia Institute of Technology

Contract with

Georgia Department of Transportation

In cooperation with

U.S. Department of Transportation
Federal Highway Administration

February, 2016

TABLE OF CONTENTS

LIST OF TABLES

Table Page No.

LIST OF FIGURES

LIST OF FIGURES

EXECUTIVE SUMMARY

During extreme hydrologic events, bridges may be subjected to submerged orifice flow and overtopping because they were not designed for such large flows. As a result, such bridges are vulnerable to excessive scour of the foundations and possible failure. The objective of this research is to examine both the hydrodynamics of the flow and the scour resistance of fine sediments to improve prediction of scour depths under extreme flooding conditions. The research approach is three-pronged: (1) experimental measurement of scour depth and flow field in a large compound channel flume; (2) application of computational fluid dynamics to predict the turbulence properties of the flow field; and (3) testing of laboratory mixtures of fine sediments to develop a relationship for critical shear stress at the threshold of scour.

While most previous research efforts aimed at the bridge scour problem have focused on one single aspect or another, this research embraces a comprehensive approach that recognizes not only the importance of predicting the hydrodynamic properties of the flow field, including turbulence, that are responsible for producing scour, but also the resisting forces of sediment erosional strength, especially in the particular case of fine sediments which experience cohesive, interparticle forces.

From the large-scale scour flume experiments, which include a realistic river cross section and bridge geometry with erodible embankments as well as an erodible river bed, it is shown that abutment and lateral contraction clear-water scour can be treated as a single process and predicted as an amplification factor times the theoretical long contraction scour. Furthermore, it is found that scour due to submerged orifice and overtopping flows can be predicted with the same approach. The amplification factor is shown to depend on the turbulent kinetic energy generated by flow separation and the zone of recirculation as the flow comes around the abutment and is constricted in the bridge section.

The computational fluid dynamics (CFD) model added a component to this research that represents a significant advance in numerical modeling of overtopping bridge flows. A state-of-the art CFD model using large-eddy simulation (LES) was applied to the overtopping flow and validated by laboratory experiments. The LES model was refined to compute the free surface position through the bridge with an accuracy not attained heretofore, and because of that it successfully predicted water surface elevations as well as levels of turbulent kinetic energy identified in the laboratory scour flume experiments as a crucial causative scour factor.

Finally, the oft-neglected sediment resistance factor in any scour process was addressed for fine sediments, which are the most difficult to characterize due to the interparticle forces binding the sediment particles. In a specially-designed erosion flume, erosion rate and critical shear stress for initiation of scour were measured for various mixtures of kaolinite clay and silt. A relationship was developed for critical shear stress in terms of sediment water content and percent clay-size fraction. In addition, yield stress of the sediment mixtures measured by a rheometer was shown to have a unique relationship with critical shear stress.

Taken together as a comprehensive approach, the results of this research provide a road map to future bridge scour research that incorporates and combines the results of realistic laboratory experiments, sophisticated numerical modeling and the essential characterization of sediment erodibility.

CHAPTER 1

INTRODUCTION

BACKGROUND

Extreme rainfall events have become more frequent in recent years and are likely to produce an increasing number of flooding scenarios resulting in inundation and infrastructure damages. During such large floods, the foundation of a bridge is subject to significant scour at the sediment bed which can cause bridge failure, especially in the case of overtopping of the embankment. In fact, bridge foundation scour is the most common cause of highway bridge failures in the U. S. (Katell and Eriksson, 1998). In the 1993 Upper Mississippi River Basin flooding, for example, the primary cause of failure at 77 percent of the bridges was scour around the abutments or approach embankments (Parola et al. 1998). Complex interactions among abutment scour, contraction scour, and pier scour occurred, especially when the bridge was inundated.

In southwest Georgia, Tropical Storm Alberto dumped as much as 71 cm of rainfall in parts of central and southwest Georgia, USA, from July 3-7, 1994 and caused numerous bridge failures and highway closings due to the 100-yr flood stage being exceeded at many locations along the Flint and Ocmulgee Rivers. A typical depth of scour was the 5.5 m of bridge foundation scour that occurred at the U.S. 82 crossing of the Flint River near Albany, Georgia (Stamey, 1996). Epic flooding with flood recurrence intervals in excess of 500 years occurred in Georgia in 2009 in the Atlanta metropolitan area with extensive damage to bridge abutments and embankments due to overtopping (Gotvald and McCallum 2010). Many small bridges were completely inundated causing the approach embankments to fail by scour with one or more spans falling into the stream in some cases.

In addition to structural damage and economic losses due to disruption of transportation, bridge failures due to scour can lead to loss of life such as in the 1987 collapse of the I-90 bridge over Schoharie Creek near Albany, New York; the US 51 bridge over the Hatchie River in Tennessee in 1989; and the I-5 bridges over Arroyo Pasajero in California in 1995 (Morris and Pagan-Ortiz 1999).

A recent survey confirmed the extent of the bridge scour problem in the U.S. (Lagasse, 2003): "*Hydraulic factors such as stream instability, degradation, contraction scour, and local scour account for more of our bridge failures (approximately 60 percent) than all other factors combined."... "On-going screening and evaluation of the vulnerability of the nations' highway bridges to scour by State Departments of Transportation have identified more than 18,000 bridges that are considered scour-critical and in need of repair or replacement".* In the State of Georgia, approximately 100 bridges have been classified as "scour-critical" (personal communication, Paul Liles), while many others are in the category of "unknown foundations" and will have to be classified according to scour vulnerability once foundation depths are established. Unfortunately, the identification of scour-critical bridges is dependent on a set of scour prediction formulas that are considered to be overly conservative in some instances. This state of engineering practice is primarily due to the following difficulties: (1) evaluating scour prediction parameters based on the forcing mechanisms of scour due to a complex turbulent flow field; and (2) estimating the scour resistance of local soils at the bridge site.

OBJECTIVE

The overall objective of the research reported herein is to identify possible improvements to scour prediction methodology by studying both the driving and resisting forces in the scour process during extreme floods. Under these conditions, complex turbulent flow patterns developed in submerged orifice flow and weir flow over bridge decks (overtopping) are likely to cause scour-critical conditions and possible bridge failure. Whether or not failure actually occurs is vitally dependent on the erosional resistance of soils relative to scour forces, but for fine-grained soils it is especially difficult to evaluate due to interparticle forces. Thus, satisfying the objective of this research demands detailed studies of scour prediction parameters and erosional strength of fine-grained soils.

RESEARCH TASKS

The research approach included both experimental and numerical methods. Specific research tasks undertaken in the research were:

(1) Utilize an existing river physical model after some modifications of the flow cross-section and sediment particle size to systematically study *simultaneous local and contraction scour* for varying erodible embankment lengths protected by riprap, especially under conditions of *submerged orifice flow, with or without overtopping,* as well as *free surface flow*;

(2) Develop a *computational fluid dynamics (CFD) model* for application to a compound channel subject to interaction between main channel and floodplain flows, and to submerged and overtopping bridge flows in which a significant variation in free surface elevation has to be modeled accurately.

(3) Test Shelby tube cores filled with *artificially mixed sediment samples* to determine yield stress from rheometer tests of the fine size fraction and relate it to the critical shear stress from corresponding flume tests of similar samples;

The results of Task 1 experiments are incorporated into a scour prediction methodology based on an amplification factor applied to theoretical contraction scour that is shown to be dependent on the flow distribution in the contracted bridge section and the properties of flow turbulence measured there. The outcome of Task 2 is a validated CFD model that incorporates the elements of bridge overtopping flow in order to identify properties of the turbulent flow field that are instrumental in causing scour. Task 3 experiments are focused on fine-grained sediments typical of those found in Georgia and are an extension of results already developed in previous GDOT-sponsored research (Sturm et al. 2008) for coarser-grained sediments obtained from field samples throughout the state of Georgia. The results of all three tasks are summarized in this report.

REPORT ORGANIZATION

The report is organized around the three research tasks listed in the research plan, and the results appear in Chapters 2, 3, and 4. These three chapters are the culmination of a comprehensive approach to bridge scour prediction and are based on the Ph.D. theses of Hong (2013), Kara (2014), and Wang (2013), respectively, which are cited throughout the report to provide additional details. In addition, these three chapters rely on a more succinct presentation of the research accomplishments in either published or submitted refereed journal articles with acknowledgment of GDOT financial support.

This report is intended to bring together under one cover these separate but related research efforts, each of which attacks a different aspect of the bridge scour research problem, in satisfaction of GDOT research deliverables for the project. Overall conclusions are provided in Chapter 5. In order to organize each chapter as self-contained, the List of Symbols and the References pertinent to each chapter are given at the end of that chapter.

REFERENCES

Gotvald, A.J. and McCallum, B.E. (2010). “Epic flooding in Georgia*,* 2009.” *U.S. Geological Survey Fact Sheet* 2010-3107, U.S. Department of the Interior, U.S. Geological Survey.

Hong, S. (2013). “Prediction of clear-water abutment scour depth in compound channel for extreme hydrologic events.” Ph.D. thesis, Georgia Institute of Technology, Atlanta, GA.

Kara, S. (2014). “Numerical simulation of flow in open-channels with hydraulic structures,” Ph.D. thesis, Georgia Institute of Technology, Atlanta, GA.

Katell, J., and Eriksson, M. (1998). “Bridge Scour Evaluation: Screening, Analysis, & Countermeasures,” United States Department of Agriculture Forest Service Technology & Development Program.” Report 7700-Transportation Systems. 9877 1207-SDTDC.

Lagasse, P. F. (2003) “Summary of 1998 Scanning Review of European Practice for Bridge Scour and Stream Instability Countermeasures”, US Department of Transportation, Federal Highway Administration, USA.

Morris, J.L., and Pagan-Ortiz, J.E. (1999). “Bridge scour evaluation program in the United States.” *Stream Stability and Scour at Highway Bridges*, E.V. Richardson and P.F. Lagasse, eds., ASCE, 61-70.

Parola, A.C., Hagerty, D.J., and Kamojjal, S. (1998). “Highway infrastructure damage caused by the 1993 upper Mississippi River basin flooding.” *Rep. No. NCHRP-417*, Transportation Research Board, Washington, D.C.

Stamey, T. C. (1996). “Summary of data collection activities and effects of flooding from Tropical Storm Alberto in parts of Georgia, Alabama, and Florida in July 1994.” *Rep. No. 96-228*, U.S. Geological Survey, Atlanta.

Sturm, Terry W., Hong, Seungho, and Hobson, Paul (2008). “Estimating critical shear stress of bed sediment for improved prediction of bridge contraction scour in Georgia,” GDOT Project 0404, Final Report, Office of Research, Forest Park, GA.

Wang, Y.-C. (2013). "Effects of physical properties and rheological characteristics on critical shear stress of fine sediments," Ph.D. Thesis, Georgia Institute of Technology, Atlanta.

CHAPTER 2

EXPERIMENTAL PREDICTION OF BRIDGE SCOUR

INTRODUCTION

As discussed in Chapter 1, the epic flood of 2009 in the southeastern sector of the Atlanta metropolitan area resulted in widespread damage to bridges primarily due to either partial or complete failure of embankments and abutments under overtopping flow conditions. In Fig. 2.1, for example, rock riprap was stripped off the spill slope of a bridge embankment, but the abutment itself remained intact and repairs were possible. In Fig. 2.2, on the other hand, bridge overtopping led to erosion of the entire left embankment with loss of the first deck span into the river; this bridge had to be replaced.

Figure 2.1. Repairable abutment damage in GA flood of 2009.

Figure 2.2 Abutment failure in GA flood of 2009.

These two examples of bridge abutment and embankment failure highlight the need for additional research in this area. Currently, no formula for abutment scour is widely applicable, nor has the term itself been distinctly defined because of difficulties in understanding the complex flow and scouring mechanisms occurring near bridge abutments in compound channels.

The scour process is initiated by flow separation from the bed as the flow approaches the obstruction offered by the embankment and abutment accompanied by downflow at the bridge obstruction. The result is a horseshoe vortex that spirals around the base of the obstruction and causes scour in conjunction with wake vortices (Paik and Sotiropoulos 2005, Koken and Constantinescu 2009, and Teruzzi et al. 2009). In addition, the bridge opening creates a flow constriction and separation of the flow as it comes around the abutment face; the location of the separation point and the size of the separated-flow zone depend on the shape and surface roughness of the abutment among other factors. For bridge abutments situated on the floodplain, the constriction results in deflection of some of the floodplain flow into the main channel and a change in flow distribution at the bridge section.

For larger floods, the flood stage may rise to the level that the bridge opening becomes submerged such that vertical contraction of the flow occurs through the bridge opening in addition to the lateral contraction of the floodplain flow. Once the bridge overtops, less flow passes through the bridge opening and the flow separation point around the abutment face may change its location. This complex flow field generates a concentrated area of scour in the vicinity of the face of the abutment where attribution of various flow processes to the total scour depth becomes problematic at best. Examples of free flow, submerged orifice flow and overtopping flow are shown in Fig. 2.3

Initial approaches to prediction of abutment scour focused on the length of the abutment as the primary independent variable (Froehlich 1989, Melville 1992). These methods relied on regression analysis of laboratory data collected primarily in rectangular channels. Laursen (1963) suggested that local abutment scour could be predicted as a multiplying or amplification factor times the theoretical long contraction scour which depended on the abutment length to determine

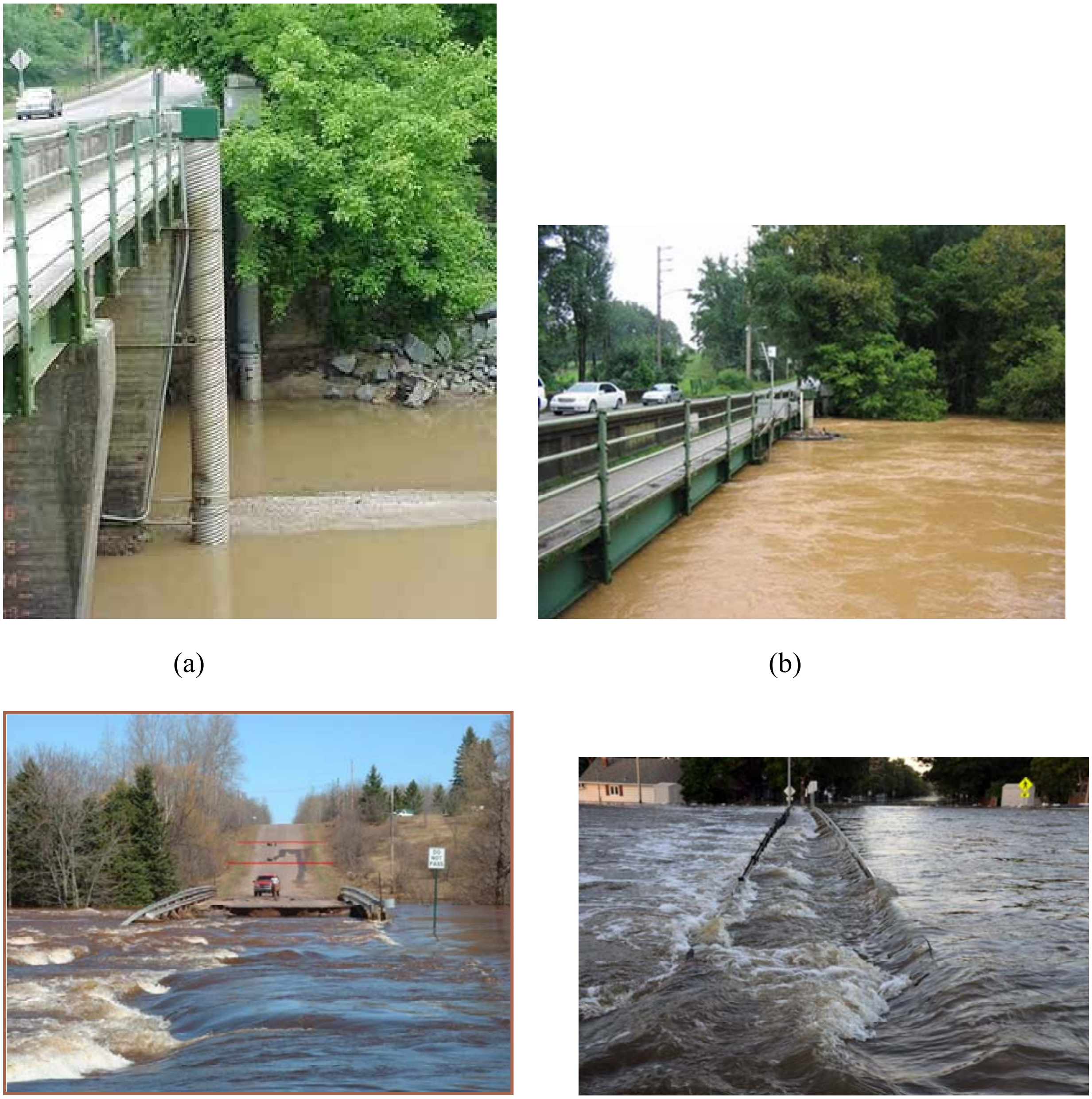

(a) (b)

(c) (d)

Figure 2.3. Types of bridge flow: (a) free flow; (b) submerged orifice flow; (c) and (d) overtopping flow.

the geometric contraction ratio. Sturm and Janjua (1994) suggested instead that the amplification factor for abutment scour in compound channels should be applied to contraction scour calculated on the basis of a discharge contraction ratio rather than the geometric contraction ratio. Later Sturm (1999, 2006) reported the results of a large number of laboratory experiments with a solid abutment in a compound channel that showed again the importance of a discharge contraction ratio. However, these scour estimates tended to be very conservative because of the use of a solid rather than an erodible embankment (Sturm et al. 2011). Another factor contributing to conservative predictions of abutment scour was the initial recommendation in HEC-18 (Richardson and Davis 2001) that abutment scour and contraction scour be added as independent contributions to the total scour. Sturm (1999) suggested that abutment scour should be considered as a combination of contraction and abutment scour. Ettema et al. (2010) conducted experiments in a laboratory compound channel with free flow around an erodible embankment and proposed amplification factors that were considerably less than those found previously for solid abutments. He also suggested that abutment and contraction scour are not independent, additive components but rather more or less important as determined by an amplification factor that varies with the discharge contraction ratio. This method is included in the most current version of HEC-18 (Arneson et al. 2012).

Further complicating the prediction of abutment scour is the occurrence of submerged orifice flow either alone or in combination with overtopping of the bridge embankment during extreme hydrologic events. In this instance, increased upstream velocities and depth can produce vertical flow contraction in addition to existing lateral flow contraction caused by the embankment on the floodplain. The result of both types of contraction is a more complex flow field in the vicinity of the abutment than for the free flow case. Although a few studies have been conducted on vertical contraction scour alone (Umbrell et al. 1998, Lyn 2008, and Guo et al. 2009), most previous studies have focused only on the case of free-surface flow in simpler idealized situations.

The main objective of this chapter is to provide an improved framework for evaluating scour potential of scour-critical bridges subject to three flow types: free flow, submerged orifice flow, and submerged orifice flow with overtopping. Physical river model experiments were conducted to investigate simultaneous local and contraction scour around an abutment in a compound channel for varying erodible embankment lengths and different flow types. It is shown that a discharge contraction ratio can unify estimates of abutment/contraction scour for all three flow types, and that the degree of erodibility of the embankment is an additional parameter to be considered in predicting abutment scour. This chapter is based on the Ph.D. thesis of Hong (2013) and the paper by Hong et al. (2015).

EXPERIMENTAL SETUP

In a previous study at the Georgia Institute of Technology (Hong and Sturm, 2009, 2010), laboratory experiments on bridge scour were conducted using a hydraulic model of the Towaliga River bridge at Macon, Georgia including the full river bathymetry. The model was constructed in a steel flume 80 ft long, 14 ft wide, and 2.5 ft deep. For the experiments reported in this chapter (Hong 2013), the Towaliga River cross-section was modified and simplified slightly to provide more general results while maintaining a realistic compound channel shape at a geometric scale of 1:45. The floodplain was made horizontal on both sides of the main channel cross-section while preserving the shape of the main channel (Fig. 2.4). The channel was also straightened in the laboratory to remove the effects of meandering. The 35 ft long fixed-bed approach flow section was filled with a 3.3 mm gravel bed in the first 17 ft followed by a 20 ft long fixed-bed section and a 17 ft long movable-bed working section consisting of sand having a median sieve diameter (d_{50}) of 1.1 mm and a geometric standard deviation of the grain size distribution of $\sigma_g = \left(d_{84}/d_{16}\right)^{0.5} = 1.3$ According to Shields' diagram, the critical value of shear velocity for initiation of motion of the sediment, u_{*c}, is 0.076 ft/s.

The model of the embankment was constructed as an erodible fill with rock riprap protection on the side slopes and a riprap apron at the toe of the embankment and the spill-through abutment in order to reproduce the influence of erosion of the abutment face in the region of the toe of the embankment (Ettema et al. 2008). The riprap was sized so as to allow some failure of the riprap apron but not of the embankment itself. First, the erodible embankment was formed by using several buckets of saturated sand (same size as bed materials) which were carefully compacted by hand and shaped using a trowel to set a 2:1 side slope. Next, the 2:1 embankment and abutment were completely covered by hand with a single layer of riprap before placing the removable model roadway and bridge deck in place. The model size of the riprap (d_{50} = 9.0 mm) was determined by the method recommended in HEC-23 (Lagasse et al. 2009) and included an apron of the recommended width of 0.56 ft in the 1:45 scale model. This approach was successful in maintaining the general integrity of the embankment during overtopping, as was observed in the prototype during an overtopping flood in 1994. A wide range of embankment lengths and flow contraction ratios were tested on the left floodplain while the abutment was maintained at the bankline of the right floodplain for all experiments as shown in Fig. 2.4. This arrangement allowed the simultaneous study of both bankline and setback abutments. The ratio of the abutment length to the floodplain width, L_a/B_f (L_a is the abutment length and B_f is the floodplain width), varied from 0.53 to 0.88 in the left floodplain and was constant at a value of 1.0 in the right floodplain. To simulate submerged orifice flow and overtopping flow cases, a model bridge deck that represented a typical four-lane bridge commonly used by the Georgia Department of Transportation (GDOT) in a rural region was constructed at a scale of 1:45. As indicated in Fig. 2.4, the prototype bridge deck had the following dimensions: a 40 ft wide roadway, in accordance with a standard two-lane road; a 2.0 ft high bridge barrier with a 1.5 ft top width; a 1.5 ft deep deck slab; and five 1.4 ft wide by 1.5 ft deep girders with 9 ft spacing.

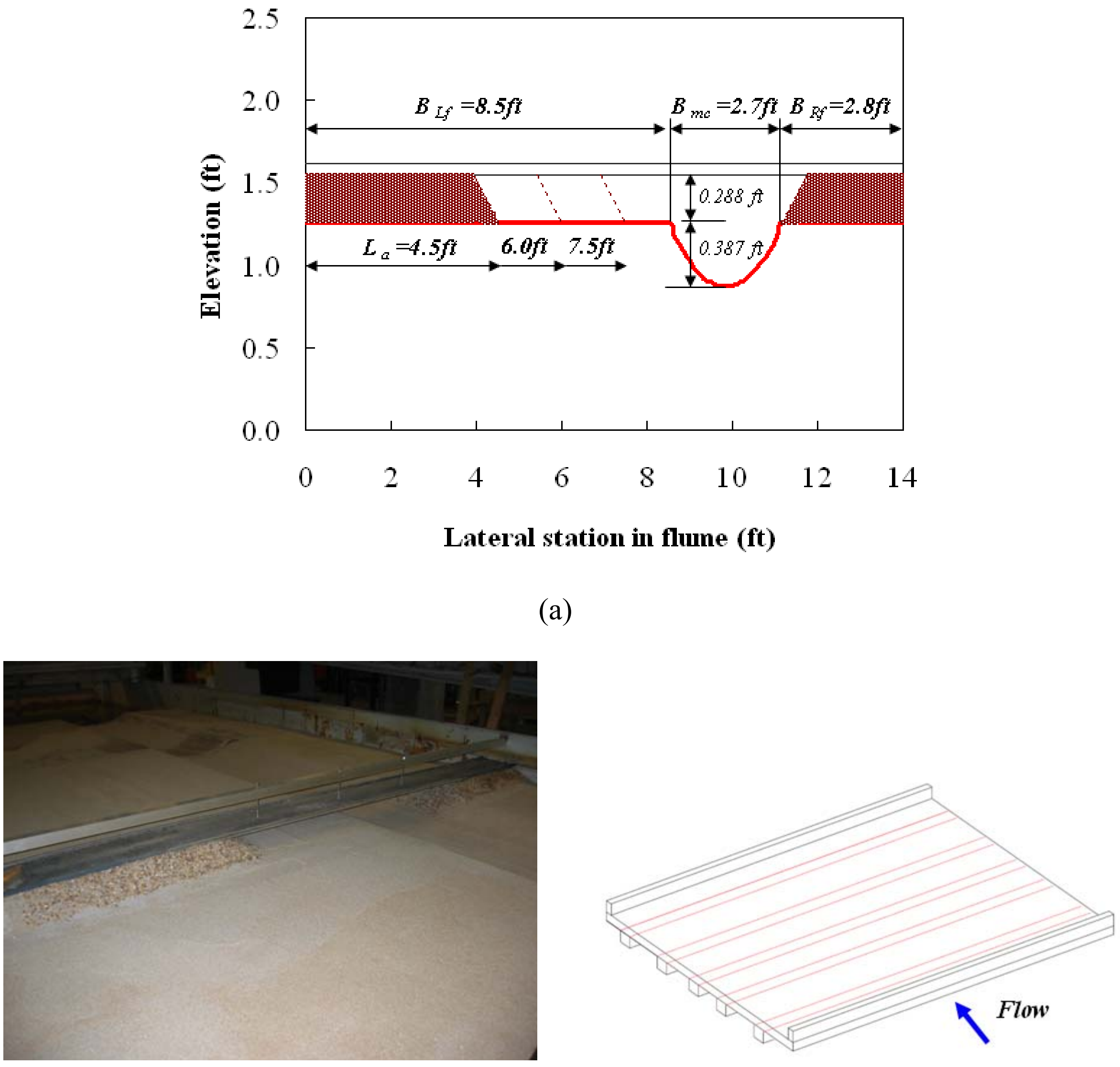

(a)

(b)

(c)

Figure 2.4. Physical model of bridge over compound channel used in all experiments: (a) bridge and compound channel cross section for variable abutment lengths in left floodplain looking downstream; (b) bridge model in 14 ft wide flume looking downstream; (c) physical model of bridge and girders (Hong 2013).

A 16-MHz MicroADV (Acoustic Doppler Velocimeter) was utilized to measure instantaneous point velocities and turbulence quantities with three different types of probes: 3D down-looking, 3D side-looking and 2D side-looking (www.sontek.com/microadv.html). When measurements were required at points close to the free surface and for shallow water depths, the 2D and the 3D side-looking ADVs were used. Accuracy of the ADV was evaluated by Voulgaris and Trowbridge (1998) in flume experiments. Their analysis showed that the ADV sensor can accurately measure both mean velocity and Reynolds stress if the signal Doppler noise is removed. Filtering protocols included requiring a minimum value of the correlation coefficient and signal-noise ratio (SNR) as recommended by the manufacturer. The phase-space despiking algorithm of Goring and Nikora (2002) was also employed to remove any spikes in the time record caused by aliasing of the Doppler signal which sometimes occurs near a boundary. Kaolin clay particles were used as seeding materials to improve the data quality. Typical correlation values in these experiments were greater than 90% and the SNR was greater than 15. The required duration of the time record at each velocity measuring point was determined to be a minimum of 2 min and as much as 5 min near the bed, and the sampling frequency was selected to be 25 Hz based on previous experiments at Georgia Tech (Lee et al. 2004, Ge et al. 2005, and Hong 2005) and guidelines suggested by Garcia (2005).

EXPERIMENTAL PROCEDURE

At the beginning of each scour experiment, the flume was slowly filled with water from a downstream supply hose so that the sand was saturated without disturbing the initial bottom contours. After complete saturation, the initial bottom elevations of the entire working movable-bed section were measured in detail throughout the test section with a spacing of 0.2 ft across each of 10 cross-sections having a streamwise spacing of 0.25 ft from the upstream to the downstream toe of the bridge embankment. With the flume flooded, but at no flow, the ADV was used to measure the bed elevations before scour relative to a fixed elevation datum established on the bottom of the flume. Subsequently, the required discharge from 2.0 to 6.0 ft^3/s was set using a magnetic flow meter (± 0.004 ft^3/s). A flow depth larger than the target value was set with the tailgate so as to prevent scour while the test discharge was adjusted. Then the tailgate was lowered to achieve the desired depth of flow. During this time, the point gage and wave gage on the instrument carriage were used to measure the flow depth. Once the target flow rate and flow depth had been reached, the scour continued for 5 to 6 days until equilibrium was achieved. Equilibrium was determined such that the bed elevation showed no change other than a fluctuation about a mean level over a period of at least 24 hr at the end of each experiment. Final bed elevations were measured in the same way as the initial elevations using the ADV and the point gage near the bridge structures.

After completion of the movable bed experiments, flat bed conditions were restored and the movable-bed section was fixed by spraying it with polyurethane. In the fixed-bed experiments, the initial hydraulic conditions for each scour experiment were obtained by measuring water-surface profiles and velocities throughout the working section. At the approach flow section, point velocities were measured along multiple vertical transects which were separated by 1.0 ft laterally in the floodplain and 0.5 ft in the main channel. Ten point velocities were taken at each vertical transect in the floodplain while measuring 15 point velocities in each vertical section in the main channel. In the bridge cross section, velocity profiles were measured every 0.5 ft laterally in both the floodplain and the main channel. A minimum of eight measuring points in each vertical profile and as many as 15 points were measured at both cross-sections

C.S. 3 and C.S. 4 (see Fig. 2.7) at the upstream and downstream faces of the bridge. In addition, three-dimensional velocity components and turbulence quantities were measured at cross sections located at the upstream toe and the downstream toe of the embankment (C.S. 2 and C.S. 5), and at C.S. 6 located 0.66 ft downstream of C.S. 5 at lateral intervals of 0.5 ft in the floodplain and the main channel. At C.S. 2, C.S. 5 and C.S. 6, three point velocities were measured in each vertical profile at distances from the bed of 0.0164 ft (5 mm), and 20 and 40 percent of the approach flow depth in both the floodplain and main channel.

DIMENSIONAL ANALYSIS

The significant parameters affecting scour at a bridge abutment located in a compound channel are obtained by dimensional analysis. A definition sketch is shown in Fig. 2.5.

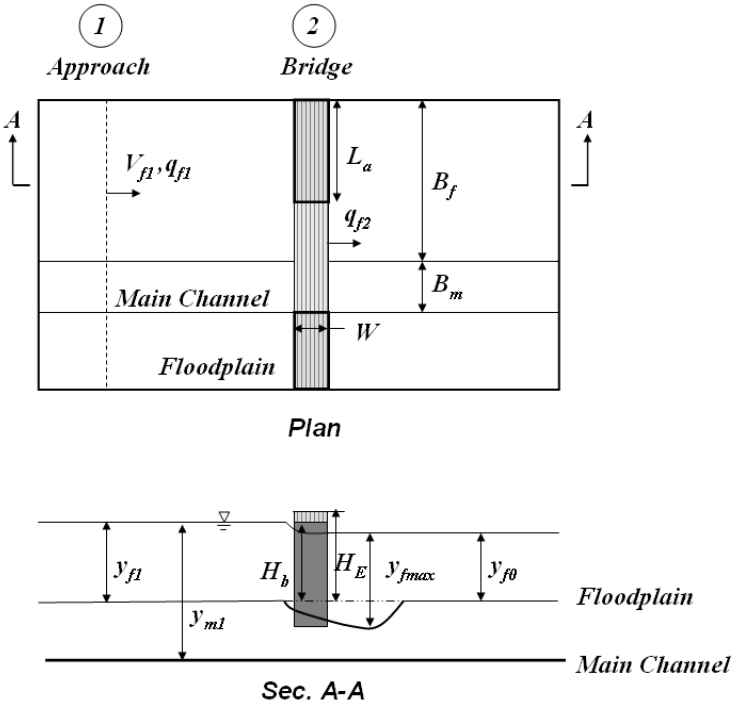

Figure 2.5. Definition sketch for scour in floodplain.

A dimensional analysis result (Sturm and Janjua 1994 and Sturm 2006) is given by

$$\frac{d_s}{y_1} = f\left(\frac{q_1}{q_2}, \frac{V_1}{V_{c1}}, \frac{y_1}{y_0}, \frac{V_1 t}{y_1}\right) \tag{2.1}$$

where $d_s = (y_{2max} - y_0)$ is the equilibrium scour depth, y_1 is the approach flow depth, q_1 is the discharge per unit width in the approach flow section, q_2 is the discharge per unit width in the bridge section, V_1 is the approach flow velocity, V_{c1} is the approach flow critical velocity, y_0 is the unobstructed flow depth at the bridge based on the tailwater elevation, and t is time. In Eq. (2.1) the subscript "*f*" for floodplain shown in Fig. 2.5 has been dropped so that the variables apply to either the floodplain or main channel depending on the location of the scour hole. Sturm (2006) and Ettema et al. (2010) applied a modified version of the long contraction theory of Laursen (1960) to justify the result indicated by Eq. (2.1) and implemented Laursen's suggestion that local abutment scour can be considered a local amplification of contraction scour as described in Eq. (2.2).

$$\frac{y_{2\max}}{y_1} = r_T\left(\left(\frac{V_1}{V_{c1}}\right)^{6/7}\left(\frac{q_2}{q_1}\right)^{6/7}\right) \tag{2.2}$$

where $y_{2\max}$ is the maximum water depth at the location of maximum scour around the abutment and r_T is an amplification term to account for the local turbulence effects that contribute to additional scour and can be determined by experiments. If significant backwater effects are expected for the design of a bridge, the backwater effect should be taken into account. For example, when the amount of obstructed discharge in the approach flow over a length equal to the abutment length is significant compared to the total discharge, the backwater may not be negligible. The dimensionless variable, y_1/y_0, which reflects the effect of backwater (Hong and Sturm 2009), is multiplied on both sides of Eq. (2.2), yielding

$$\frac{y_{2\max}}{y_0} = r_T\left(\frac{y_1}{y_0}\right)\left(\left(\frac{V_1}{V_{c1}}\right)^{6/7}\left(\frac{q_2}{q_1}\right)^{6/7}\right) \tag{2.3}$$

If a significant backwater effect is expected for the design of a bridge, y_0 should be used for the reference flow depth; otherwise, approach flow water depth y_1 can be used instead of y_0 in Eq. (3) because the value of y_1/y_0 is close to 1.

RESULTS AND DISCUSSION

Fixed Bed Experiments

The depth-averaged, streamwise velocities in the approach flow cross section were determined by application of the best fit of the logarithmic velocity profile to the measured point velocities in the vertical. The depth-averaged velocity was then evaluated from the best-fit log relationship. However, in the bridge section, the depth-averaged velocities were calculated by taking the integral of the point velocity measurements within each vertical velocity profile over the depth and dividing by the water depth because the velocity profiles in the bridge section did not have a logarithmic relationship due to the complex three-dimensional flow behavior there.

The experimental conditions measured in the fixed bed are shown in Table 2.1 in terms of dimensionless parameters. These parameters include the ratio between abutment length and floodplain width in the left floodplain, L_a/B_f; total discharge, Q; the approach flow intensity in the floodplain and main channel, respectively, V_{f1}/V_{fc1} and V_{m1}/V_{mc1}; and the unit discharge contraction ratio measured across C.S. 4 at the downstream face of the bridge for the floodplain and main channel, respectively, q_{f2}/q_{f1} and q_{m2}/q_{m1}. As shown in Table 2.1, in the first three experimental runs, the flow intensity parameter, V_{f1}/V_{fc1}, in the left floodplain had a similar value so that the effect of different flow types in clear-water scour could be examined. The same procedure was applied in the other experiments. The experiments were conducted such that the three flow types of free flow (F), submerged orifice flow (SO), and overtopping flow (OT) were encountered for increasing *Q* while simultaneously increasing the tailwater such that the value of V_{f1}/V_{fc1} remained nearly constant. The value of q_2/q_1 at C.S. 4 is used in the scour formula suggested subsequently because it represents the maximum contraction at the downstream face of the bridge.

Table 2.1. Summary of experimental conditions and results (Hong 2013).

Run	*Flow type*	*Q* *(ft³/s)*	$\frac{L_a}{B_f}$ **	$\frac{V_{f1}}{V_{fc1}}$	$\frac{q_{f2}}{q_{f1}}$	$\frac{y_{f\max}}{y_{f0}}$	$\frac{L_a}{B_f}$ ***	$\frac{V_{m1}}{V_{mc1}}$	$\frac{q_{m2}}{q_{m1}}$	$\frac{y_{m\max}}{y_{m0}}$
1	F	3.3	0.53	0.61	1.818	3.197	1.0	0.83	1.543	2.177
2	SO	4.1		0.60	1.875	3.000		0.73	1.483	1.986
3	OT	5.8		0.61	1.148	2.295		0.72	1.146	1.540
4	F	3.0		0.58	1.755	3.032		0.77	1.441	1.830
5	SO	3.9		0.57	1.781	2.818		0.68	1.416	1.742
6	OT	5.3		0.56	1.250	1.807		0.64	1.100	1.318
7	F	3.0	0.71	0.54	2.236	3.295	1.0	0.74	1.756	2.191
8	SO	3.65		0.53	2.257	3.070		0.71	1.602	2.007
9	OT	5.3		0.56	1.176	2.090		0.66	1.243	1.534
10	F	2.6		0.49	2.208	2.900		0.72	1.539	1.800
11	SO	3.2		0.49	2.223	2.753		0.61	1.647	1.922
12	OT	4.6		0.50	1.278	1.845		0.57	1.262	1.435
13	F	2.6	0.88	-	-	1.973*	1.0	0.69	1.904	1.931
14	SO	3.1		-	-	2.289*		0.63	1.951	2.181
15	OT	4.6		-	-	1.523*		0.57	1.422	1.324
16	F	2.2		-	-	1.647*		0.55	1.976	1.866
17	SO	2.6		-	-	1.900*		0.52	1.902	1.990
18	OT	3.9		-	-	1.283*		0.50	1.481	1.219

Note: Flow type: F=free flow; SO=submerged orifice flow; OT=overtopping flow; *The maximum water depth in the left floodplain for L_a/B_F =0.88 was normalized by the main channel water depth; ** L_a/B_f in the left floodplain; *** L_a/B_f in the right floodplain.

Classification of Scour Conditions

Several conditions of abutment scour can develop in accordance with the flow field that develops at an abutment subject to the physical shape and erodibility characteristics of the embankment and abutment, and the relative location of the abutment in the waterway which usually has a compound channel geometry. In this study, scour conditions are classified into three cases based on the location of the maximum scour hole depth relative to the toe of the abutment and the bank of the main channel for spill-through, erodible embankments protected by rock riprap including a riprap apron. To distinguish whether the scour hole occurs in the floodplain or the main channel, W/y_{f1} is compared with L_m/y_{f1}, where W is the distance from the toe of the abutment in the floodplain to the bank of the main channel, and L_m is the transverse distance from the toe of the abutment to the maximum scour hole depth. The maximum value of L_m/y_{f1} in all experiments was 5.84. Thus, if the value of W/y_{f1} is larger than approximately 6, the location of the maximum scour hole depth is expected to be within the floodplain, and the scour condition is classified as long setback abutment (LSA) scour (L_a/B_f = 0.53 and 0.77 in this study). However, if the value of W/y_{f1} is smaller than approximately 6, the scour condition is classified as short setback abutment (SSA) scour (L_a/B_f = 0.88 in this study) because the location of maximum scour is in the main channel. Finally, L_a/B_f = 1.0 in this study is a bankline abutment (BLA).

Effect of Different Flow Types on Scour Depth

Fig. 2.6 shows bed elevation contours at the end of scouring for runs 1, 2, and 3. As shown in Table 2.1, experimental runs 1, 2, and 3 were conducted with the same value of L_a/B_f and V_{f1}/V_{fc1} in the floodplain, but had different flow types (F, SO, and OT). As time progressed, the

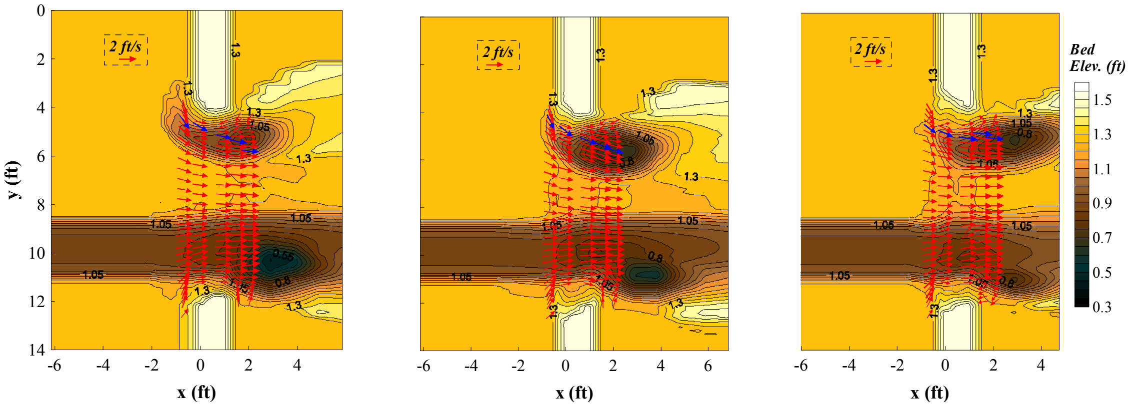

(a)

(b)

(c)

Figure 2.6. Scour contours and velocity vectors before scour in Run 1 (free flow), Run 2 (submerged orifice flow) and Run 3 (overtopping flow) for $L_a/B_f = 0.53$ (Hong 2013). Blue line represents track of maximum scour depth with time.

locus of maximum scour depth curved around the abutment, and moved from the upstream corner of the abutment face to a point that was diagonally displaced in the downstream direction from the downstream toe of the abutment for free flow and submerged orifice flow. However, for overtopping flow, the scour hole was further elongated in the streamwise direction by comparison, and the resulting point of maximum scour moved in the streamwise direction to a point further downstream of the abutment. For the bankline abutment, the maximum scour depth occurred in the vicinity of the main channel bankline downstream of the bridge.

The location of maximum scour depth and the shape of the scour hole, can be explained in part by the flow field around the abutment prior to scour. Fig. 2.6 displays the distribution of velocity vectors measured before scour in a horizontal plane located 5 mm above the fixed bed superimposed on the final bed elevations after scour. The long roadway approach section and the narrow bridge opening forced the floodplain flow to be constricted through the bridge opening, resulting in deflection around the upstream corner of the abutment and flow separation. The thalweg of the maximum scour hole depth developed with time along the trajectory of the streamlines. The streamwise velocity components increased in the longitudinal direction through the bridge, and recirculating eddies can be seen downstream of the embankment due to separation and entrainment in the cases of free flow and submerged orifice flow. The maximum scour depth at equilibrium occurred immediately downstream of the bridge in the jet-like flow caused by lateral contraction and flow separation. For overtopping flow, however, the streamlines were more nearly aligned with the longitudinal flow direction due to a portion of the blocked flow going over the embankment and roadway. The scour hole extended further downstream as the jet-like flow expanded downstream of the embankment and the lateral recirculation zone was pushed further downstream. The formation of a surface jet and recirculating eddy in the vertical plane due to overtopping may also contribute to the elongated scour hole, but this requires further investigation. The ratio of the overtopping discharge to the total discharge varied from 0.36 to 0.41 in these experiments. In any case, it seems that the non-uniformity of scour depth across the floodplain cannot be explained by the velocity vectors in a horizontal plane near the bed alone; rather, it is likely the cumulative result of the complex three-dimensional flow that is occurring there.

Assessment of the Local Turbulence Effect

In addition to the flow contraction effect described in the previous section, the horseshoe vortex is also thought to play a role in the scour process around the abutment. This contribution can be considered a local flow phenomenon with a changing relative contribution to the total abutment/contraction scour (Ettema et al. 2010, Sturm et al. 2011). Because both contributions result in increased turbulence near the bed, this section focuses on a connection between equilibrium scour depths and the initial (before scour) spatial distribution of maximum turbulent kinetic energy (TKE) near the channel bed. In each vertical profile, the maximum values of TKE were observed at the near-bed measurement location. As shown in Figs. 2.7, 2.8, and 2.9, the magnitude of TKE near the bed, non-dimensionalized by the approach flow shear velocity, u_{*1}, increased in the downstream direction from C.S. 3 to C.S. 5. Although the maximum TKE near the bed was approximately the same in the floodplain at C.S. 5 and 6 for Run 1, the maximum value occurred at C.S. 5 (in line with the downstream toe of the embankment) in all other cases including different embankment lengths and for all three flow types. The peak value of TKE increased in going from free to submerged orifice to overtopping flow to values as high as K_b/u_{*1} ~ 80 to 100, but the lateral distribution became more concentrated at the peak for overtopping flow. Because the values of K_b/u_{*1}^2 tended to be elevated above a background value over the full width of the scour hole, a spatial cross-sectional average indicated by $\overline{K}_b/u_{*1}^2$ was taken across the equilibrium width of scour hole, as illustrated in Fig. 2.7 between the dimension lines, and was tested as a possible surrogate for the complex local effects of turbulence on scour hole development. The elevated value of TKE near the bed has been suggested previously as an important variable to account for the impact of the local turbulence energy on the scour around an abutment (Chrisohoides et al. 2003, Ge et al. 2005, and Lacey and Rennie 2012).

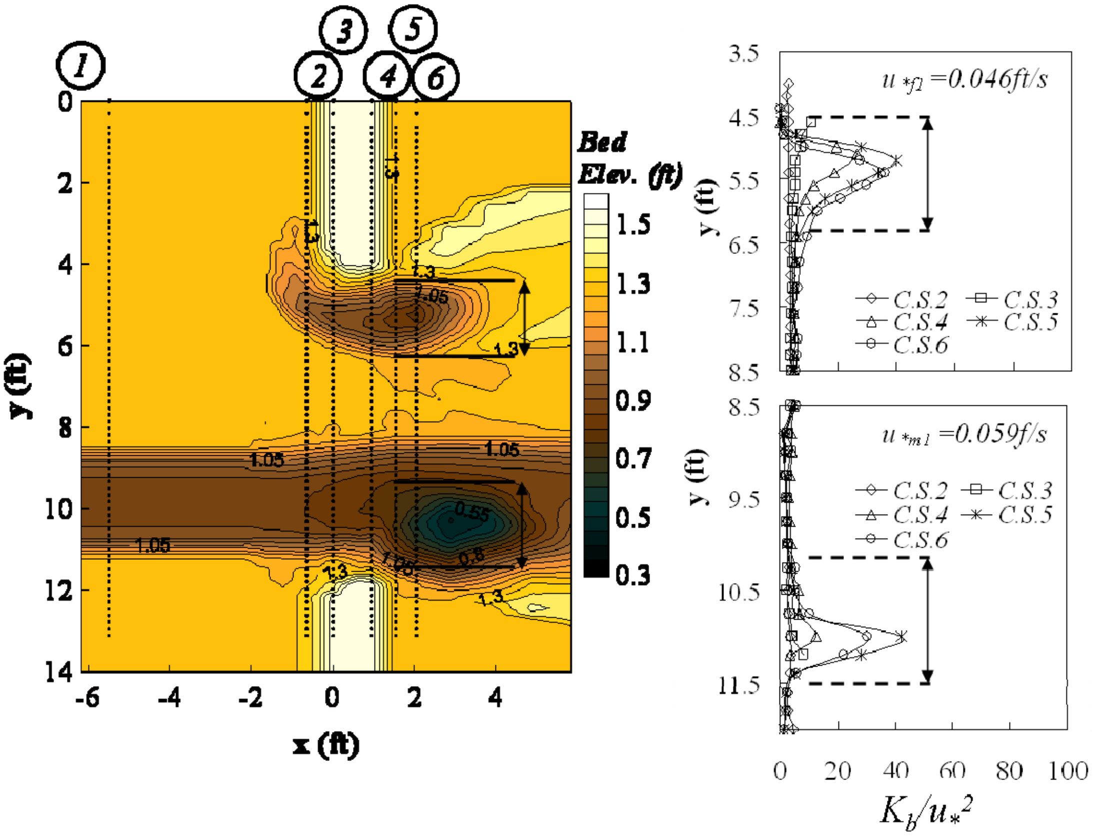

Figure 2.7. Point turbulent kinetic energy distribution near the bed and width-averaged turbulent kinetic energy across the width of the scour hole at CS 5 for Run 1, free flow (Hong 2013).

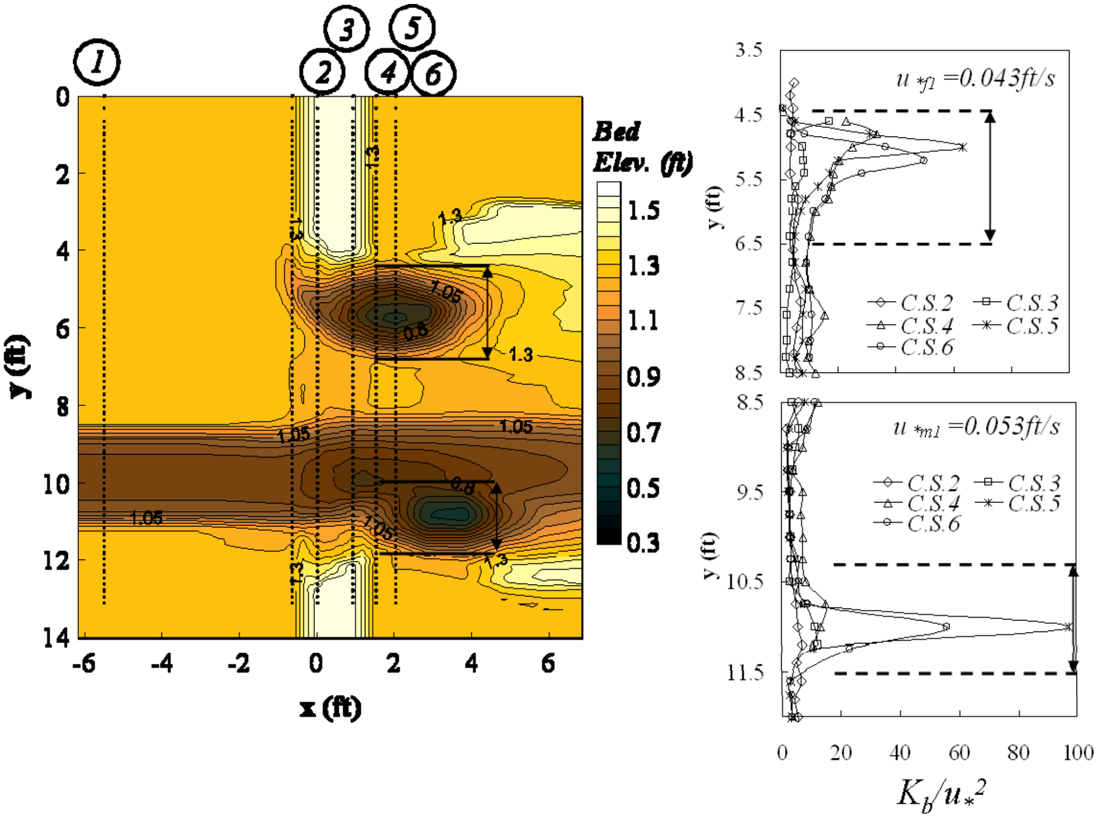

Figure 2.8. Point turbulent kinetic energy distribution near the bed and width-averaged turbulent kinetic energy across the width of the scour hole at CS 5 for Run 2, submerged orifice flow (Hong 2013).

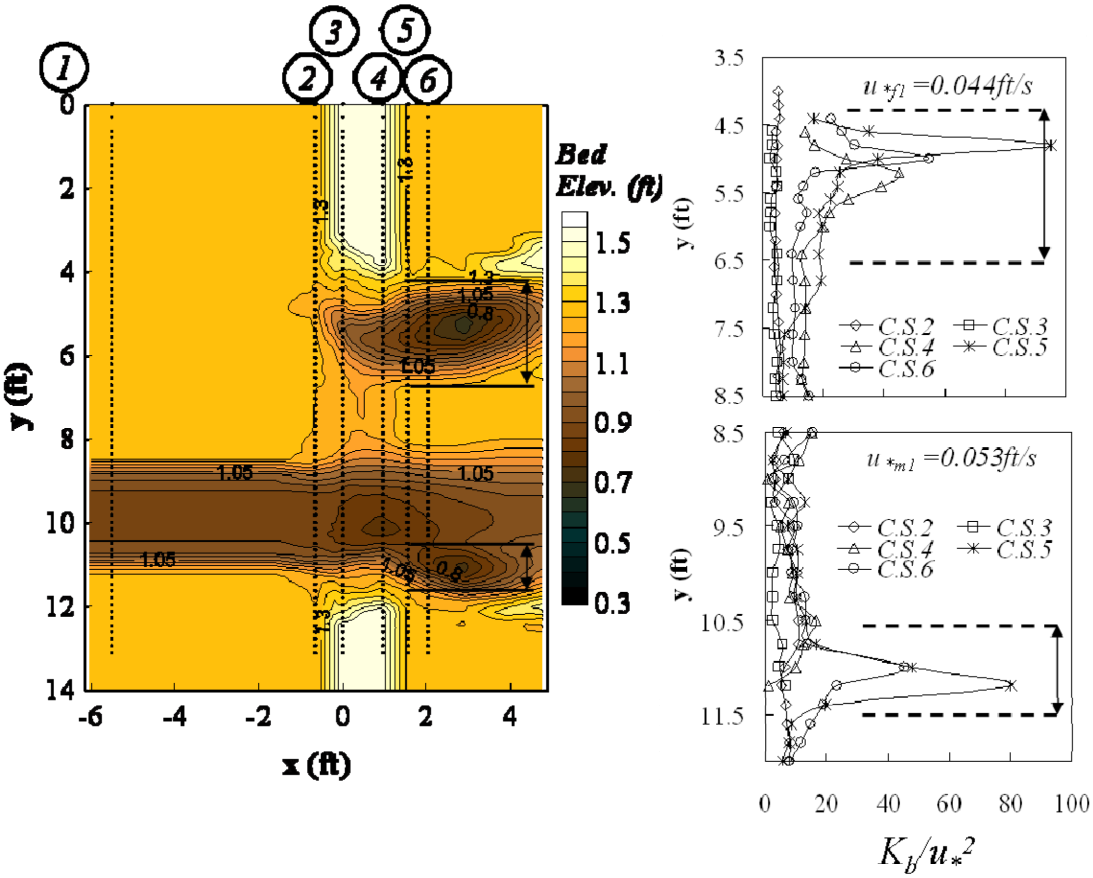

Figure 2.9. Point turbulent kinetic energy distribution near the bed and width-averaged turbulent kinetic energy across the width of the scour hole at CS 5 for Run 3, overtopping flow (Hong 2013).

As shown in Fig. 2.10, $\overline{K}_b/u_{*1}^2$ values at C.S. 5 decreased with q_2/q_1 as the degree of flow constriction increased for both long-setback abutments (LSA) and bank-line abutments (BLA). Values of $\overline{K}_b/u_{*1}^2$ were larger for overtopping flow perhaps because of the flow cascading over the bridge deck and creating increased turbulence energy. If $\overline{K}_b/u_{*1}^2$ can be interpreted as the net result of the increased turbulence energy due to the local effects of the horseshoe vortex, separated shear layer, and overtopping, when it occurs, then its decreasing magnitude with greater flow constriction is consistent with a reduced influence of the local turbulence amplification factor (r_T) for abutment/contraction scour at severely contracted bridge openings and a greater influence of the acceleration due to flow constriction. This concept relative to scour depth prediction is explored in the next section.

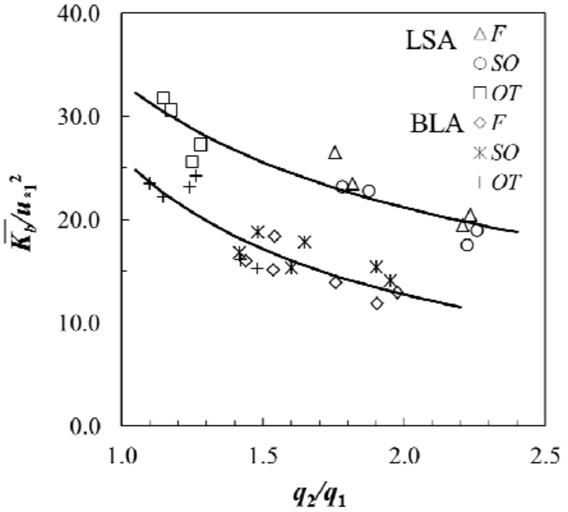

Figure 2.10. Variation of width-averaged TKE ($\overline{K}_b/u_*^2$) with discharge contraction ratio (q_2/q_1) (Hong 2013).

Analysis of Maximum Scour Depth Around an Abutment

The effects of lateral and/or vertical flow contraction and local turbulence all contribute to scour around an abutment. As a result, it is hypothesized that the maximum scour depth around an abutment can be predicted by an amplification factor due to local turbulence effects applied to the theoretical long-contraction scour as first suggested by Laursen (1960) as shown in Eq. (2.3). What has not been tried previously is to apply this concept to not just free flow through a bridge, but also to submerged orifice flow and overtopping flow provided that both the vertical and lateral flow contraction effects can be parameterized by the ratio, q_2/q_1, the ratio of discharge per unit width under the bridge to that in the approach flow. In addition, it is shown herein that the amplification ratio r_T is not a constant but rather a variable that changes with the relative contribution of the local turbulence to the overall scour depth. In the following analysis, r_T is related to a lateral, spatial average of the measured turbulent kinetic energy, $\overline{K}_b/u_{*1}^2$, before scour immediately downstream of the bridge where the scour hole develops.

The measured maximum abutment/contraction scour depths are plotted in Fig. 2.11(a) and 2.11(b) for the long setback abutment (LSA) and the bankline abutment (BLA), respectively, according to the dimensionless variables suggested by the theoretical contraction scour analysis given by Eq. (2.3). As shown in Fig. 2.11, as the dimensionless variable, $(y_1/y_0)[(V_1/V_{c1})(q_2/q_1)]^{6/7}$, on the *x*-axis increases, normalized scour depth gradually increases albeit at a decreasing rate. The results confirm that maximum abutment scour can be considered a multiple of contraction scour effects instead of an addition of local and contraction scour components that are incorrectly assumed to be independent. The measured scour depths seem to follow the same trend in Figs. 2.11, even if they have different flow types. Although the observed data for overtopping flow are in a slightly lower range than the other two flow types, regression analysis shows a continuous relationship in both figures. As Q increases, overtopping occurs and relatively less flow goes under the bridge so that q_2/q_1 is less.

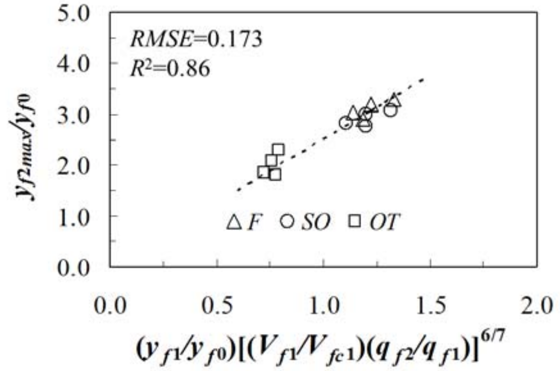

(a)

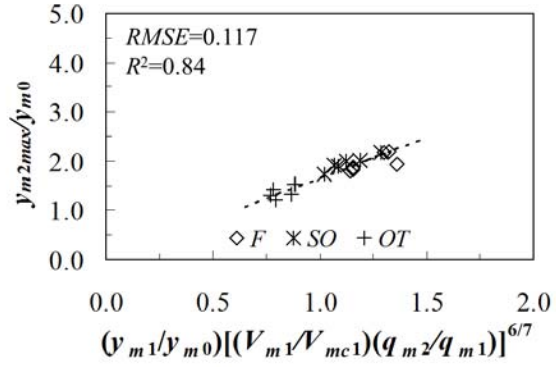

(b)

Figure 2.11. Normalized scour depth, $y_{\max}/y_0$, as a function of $(y_1/y_0)\left[(V_1/V_{c1})(q_2/q_1)\right]^{6/7}$ for (a) LSA and (b) BLA (Hong 2013).

The best-fit lines shown in Fig. 2.11 are for a constant value of r_T. In the case of the long-setback abutment (LSA), r_T = 2.51 while it is 1.66 for the bankline abutment (BLA). The best-fit statistics are given in the figure. Constant values of r_T implicitly suggest that the contribution of local turbulence effects to the total abutment scour is unchanged as the discharge contraction ratio increases. For a number of reasons, this preliminary result is oversimplified. First, in terms of limiting cases, the very short abutment, which in reality is a half-pier on a sidewall, experiences scour that is driven primarily by the dynamics of the horseshoe vortex (Koken and Constantinescu, 2006) alone. The very long abutment, on the other hand, experiences scour dominated by flow contraction (Sturm et al. 2011). Second, for an erodible abutment, the degree of scour protection afforded by failure of the riprap as it slides into the scour hole suggests that abutment scour relative to the theoretical long contraction scour should decrease as q_2/q_1 increases assuming that total riprap and embankment failure do not occur. Finally, the data trends in Fig. 2.11 suggest a decreasing slope with increasing values of q_2/q_1. In summary, r_T is not necessarily expected to be constant over a larger range of the independent variables as limiting cases are approached because the relative effect of turbulence will be different depending on the abutment length, the approach flow velocity distribution, the flow types, and the compound channel geometry.

Under these circumstances, parameterizing the role of turbulence through its structure seems challenging, but it is hypothesized that the contribution of the turbulence is an increase in TKE at the bed that provides the energy and necessary pressure fluctuations for initiating motion and sustaining sediment transport to create a scour hole. The relative contribution of local turbulence could be expected to dominate the scour process for a short abutment, as for a pier, and be overpowered by the flow contraction in the case of a long abutment. As noted previously, the maximum value of width-averaged TKE was observed at C.S. 5, where flow contraction was the greatest and a higher-velocity shear flow occurred. Accordingly, the value of width-averaged TKE ($\overline{K}_b/u_*^2$) at C.S. 5 was tentatively selected as a representative parameter to account for the local turbulence effect on the maximum abutment scour depth. The data given in Fig. 2.11, and the measured values of $\overline{K}_b/u_*^2$ at C.S. 5, were used to conduct a regression analysis for the LSA and BLA. The results are given by Eqs. (2.4) and (2.5):

$$\frac{y_{f2\max}}{y_{f0}} = 0.96\frac{y_{f1}}{y_{f0}}\left(\frac{\overline{K_b}}{u_*^2}\right)^{0.31}\left(\left(\frac{q_{f2}}{q_{f1}}\right)\left(\frac{V_{f1}}{V_{fc1}}\right)\right)^{6/7} \qquad \text{for LSA} \qquad (2.4)$$

$$\frac{y_{m2\max}}{y_{m0}} = 0.92\frac{y_{m1}}{y_{m0}}\left(\frac{\overline{K_b}}{u_*^2}\right)^{0.21}\left(\left(\frac{q_{m2}}{q_{m1}}\right)\left(\frac{V_{m1}}{V_{mc1}}\right)\right)^{6/7} \qquad \text{for BLA} \qquad (2.5)$$

for which coefficients of determination are 0.98 and 0.92, and standard errors in $y_{\max}/y_0$ are 0.088 and 0.086, for the LSA and the BLA, respectively. Eqs. (2.4) and (2.5) result in an increase in the value of the coefficient of determination from 0.86 to 0.98 and from 0.84 to 0.92 for the LSA and the BLA, respectively, in comparison with constant values of r_T. Furthermore, the standard errors of estimate for the relative scour depth are almost half of the corresponding values for constant r_T. The values of r_T from Eqs. (2.4) and (2.5) vary from 2.8 to 2.3 and 1.8 to 1.5 as the flow contraction ratio (q_2/q_1) increases from 1.1 to 2.3 and 1.1 to 2.0 for the LSA and BLAs, respectively. In other words, r_T reflects a larger influence of local turbulence energy on scour for the case of a short abutment terminating on the floodplain and a decreasing relative effect as the flow contraction becomes more severe with increasing abutment length.

By virtue of the relationship between $\overline{K}_b/u_*^2$ and q_2/q_1 given in Fig. 2.10, r_T can be determined as a function of q_2/q_1 alone. Again based on Eq. (2.3), the regression results are:

$$r_T = 2.75\left(\frac{q_{f2}}{q_{f1}}\right)^{-0.16} \qquad \textit{for LSA} \qquad (2.6)$$

$$r_T = 1.75\left(\frac{q_{f2}}{q_{f1}}\right)^{-0.12} \qquad \textit{for BLA} \qquad (2.7)$$

For these relationships, the coefficients of determination are R^2 = 0.94 and 0.87, and standard errors in $y_{\max}/y_0$ are 0.132 and 0.111 for the LSA and for the BLA, respectively. While the best fit is not quite as good as Eqs. (2.4) and (2.5), it is better than for constant values of r_T and does not require evaluation of $\overline{K}_b / u_*^2$.

Scour Prediction for a Short Setback Abutment (SSA)

In the foregoing analysis of scour depths, the LSA defines one extreme in which the scour hole remains in the floodplain while the BLA is the other extreme for which maximum scour depths occur in the main channel with concomitant instability of the bank of the main channel. For these two cases, floodplain approach flow variables and main channel approach flow variables are used for the characteristic scales to calculate the non-dimensional independent parameters for LSA scour and BLA scour, respectively. However, it is unclear how to choose the characteristic scales when the initial scour occurs in the floodplain, while the maximum equilibrium scour depth is observed in the main channel because both floodplain and main channel approach flow variables (and their interaction) are contributing to the scour process. For the purpose of this study, main channel approach flow variables were selected for the calculation of the normalized independent scour parameters for the short setback abutment (SSA) because maximum scour occurred in the main channel for this case. Furthermore, the experimental data from the SSA seem to follow the same trend as those from the BLA.

Scour depth results for the SSA were compared with BLA data with the measured flow depth at the point of maximum scour is normalized by the approach main channel flow depth on the y-axis for both cases. Based on this comparison, Eq. (2.5) or Eq. (2.7) for the BLA is recommended for the SSA even though it overestimates the measured scour depths by 6 to 13%. More data are needed to better define this case.

Comparison with Other Investigators' Results

The maximum scour depths measured near the abutment were compared with the experimental data of two other investigators (Sturm 2006 and Ettema et al. 2010) whose experiments were conducted in a compound channel with several different lengths of fixed abutments (Sturm 2006) and erodible abutments (Ettema et al. 2010) in the free flow condition with spill-through abutment geometry. Their suggested scour prediction methods were derived based on dimensional analysis and the theoretical long contraction as in this research.

The data from LSA experiments in this study are plotted along with Sturm (2006) and Ettema et al. (2010) in terms of the non-dimensional approach flow floodplain variables in Fig. 2.12. In the erodible abutment experiments (i.e., this study and Ettema et al. 2010), the non-dimensional maximum scour depth gradually increased at a decreasing rate and reached a constant value for large values of the independent variable shown on the *x*-axis. However, results from the solid abutments follow almost a linear trend with the independent non-dimensional variable and show a much larger value of the normalized maximum scour depth than those from the erodible abutments. This comparison confirms that solid and erodible abutments behave differently during the scour process. The solid abutment without a riprap apron remained intact during the scour experiments, and the resulting maximum scour hole occurred around the upstream toe of the abutment. For the erodible abutment, however, the resulting region of deepest scour was observed at the downstream side of the abutment because of sliding of part of the riprap apron into the scour hole as explained previously. The importance of embankment erosional strength can be further highlighted by comparing results from this study and those of Ettema et al (2010) in Fig. 2.12. Results from this study showed a slightly larger scour depth than those from Ettema et al. (2010), even though the experimental data appear to follow a similar trend. This observation might be explained by slightly different erosional strengths of the erodible embankments in the two studies.

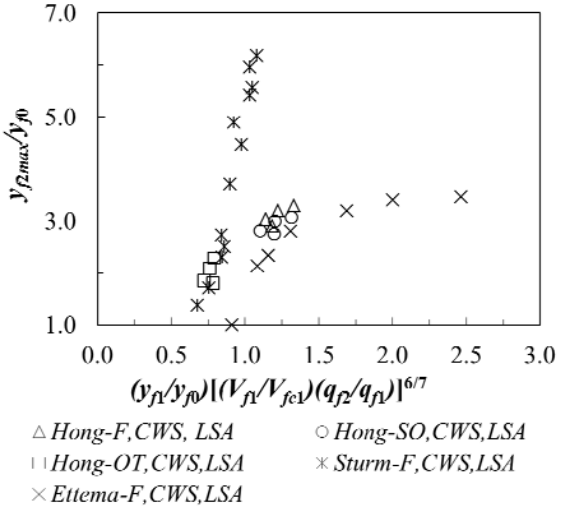

Figure 2.12. Comparison with other investigators' results for the long setback abutment (Note: Flow type: F=free flow; SO=submerged orifice flow; OT=overtopping flow; CWS=clear-water scour; LSA=long setback abutment) (Hong 2013).

Fig. 2.13 shows a comparison of scour data from different sources for BLAs. In contrast to the LSA results, the data for solid abutments are similar to those for erodible abutments in the case of the BLA. For the LSA, maximum scour occurred around the downstream side of the abutment for an erodible embankment and at the upstream corner of the abutment for a solid abutment, respectively. Maximum scour for the erodible BLA still occurred around the downstream side of the abutment, but for the solid BLA, the maximum point was located in the main channel and laterally displaced from the abutment face rather than at its upstream corner. For the BLA, severe flow contraction plays a greater role in the development of maximum scour depth than the local flow structure around the abutment. As a result, the erosional strength of the embankment becomes less important for BLA scour because it is farther away from the abutment rather than at its upstream corner. The scour depth results of Ettema et al. (2010) for BLA are slightly smaller than in this study perhaps because their scour conditions were live-bed.

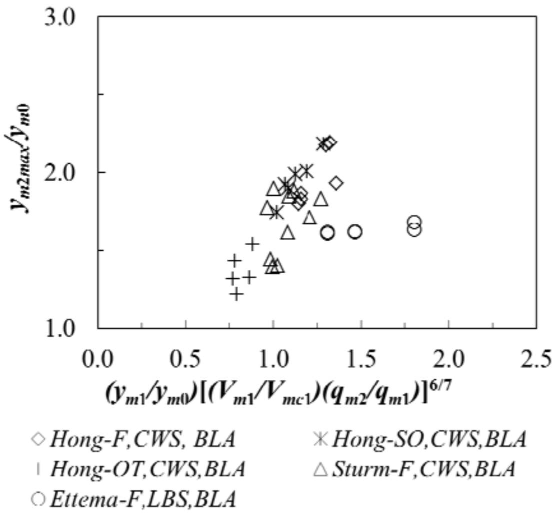

Figure 2.13. Comparison with other investigators' results for the bankline abutment (Note: Flow type: F=free flow; SO=submerged orifice flow; OT=overtopping flow: CWS=clear-water scour; LBS=live-bed scour; BLA=bankline abutment).

This study has established upper and lower limits on abutment scour based on whether the embankment is solid or erodible and protected by rock riprap. In the short term, while further studies of the effect of embankment erosional strength are made, it is recommended that abutments be set back from the bank of the main channel and protected by a rock riprap blanket and apron designed as indicated in HEC-23 (Lagasse et al. 2009). The amount of the setback based on this study should be at least $6y_{f1}$.

APPLICATION OF RESULTS

It is recommended that combined abutment/contraction scour be calculated from Eq. (2.3) using the best-fit relationship for r_T given by Eqs. (2.6) and (2.7). The procedure can be summarized as follows:

1. Determine approach flow independent hydraulic variables in floodplain and main channel using HEC-RAS.

2. Determine if abutment is long setback, LSA, ($W/y_{f1} > 6$) or short setback, SSA, ($W/y_{f1} < 6$) where W = setback distance from toe of abutment to bank of main channel and y_{f1} = approach flow depth in floodplain. For LSA, use flow variables in floodplain with scour hole in floodplain, while for SSA and bankline abutments (BLA), all independent variables should be based on main channel values with the scour hole occurring in the main channel.
3. Calculate approach flow intensity (V_1/V_{c1}) with V_1 in the floodplain for a LSA and in the main channel for a BLA or SSA. The critical velocity is obtained from the sediment properties.
4. Determine unit discharge contraction ratio (q_2/q_1) directly from HEC-RAS, again for a LSA or SSA and BLA.
5. Overtopping discharge can be calculated by the broad-crested weir equation in step 4 with q_2/q_1 calculated for flow under the bridge. HEC-RAS will also give the overtopping discharge from the broad-crested weir equation, but it will need to be computed separately for the floodplain and main channel.
6. r_T can be estimated from q_2/q_1 by Eq. 2.6 or Eq. 2.7 and substituted into Eq. 2.3 to obtain the flow depth at the maximum depth of scour.

SUMMARY

In this research, free flow, submerged orifice flow, and overtopping flow have all been imposed on a realistic bridge and compound channel geometry in a large laboratory flume. Detailed scour depth contours, velocity, and turbulent kinetic energy were measured at several cross-sections in the vicinity of the bridge. It has been shown in all three types of flow with long setback, short setback, and bankline abutments that scour depth can be predicted as an amplification factor times the theoretical long contraction scour. Furthermore, the amplification factor is shown to depend on the turbulent kinetic energy generated by flow separation around the bridge abutment section, but also that an estimate of the amplification factor can be obtained as a function of the flow contraction ratio, q_2/q_1. Based on this insight, a scour prediction procedure was developed for combined abutment and contraction scour under clear-water conditions

LIST OF SYMBOLS

B_f	width of floodplain in compound channel;
B_{mc}	width of main channel;
d_{16}	16 percent finer sediment size;
d_{50}	median diameter of sediment;
d_{84}	84 percent finer sediment size;
d_s	equilibrium abutment scour depth;
F	free flow;
H	water depth;
K	measured total turbulent kinetic energy = $0.5\left(< u'^2 > + < v'^2 > + < w'^2 >\right)$ in which $\sqrt{< u'^2 >}$, $\sqrt{< v'^2 >}$, and $\sqrt{< w'^2 >}$ are longitudinal, lateral, and vertical turbulence intensity, respectively;
K_b	total turbulent kinetic energy near the bed ;
$\overline{K}_b$	width-averaged total turbulent kinetic energy near the bed;
k_s	equivalent sand grain roughness height ;
k_s^+	dimensionless equivalent sand grain roughness height;
L_a	abutment/embankment length;
L_m	transverse distance from the toe of the abutment to the maximum scour depth;
OT	overtopping flow;
Q	total discharge in compound channel;

Q_{ot}	overtopping discharge in bridge section;
q_1	flow rate per unit width in the approach flow section;
q_2	flow rate per unit width through the bridge section;
q_{f1}	flow rate per unit width in approach flow floodplain;
q_{f2}	flow rate per unit width through the bridge section floodplain;
q_{m1}	flow rate per unit width in approach flow main channel;
q_{m2}	flow rate per unit width through the bridge section main channel;
r_T	amplification coefficient to account for local turbulence effects;
SO	submerged orifice flow ;
TKE	turbulent kinetic energy ;
t	time since beginning of scour;
U	time-averaged point velocity;
u_*	shear velocity;
u_{*1}	shear velocity of approach flow;
u_{*c}	critical value of the shear velocity;
V_1	mean velocity of approach flow;
V_c	critical velocity corresponding to initiation of sediment motion;
V_{c1}	critical velocity of approach flow;
V_{f1}	mean velocity in approach flow floodplain;
V_{fc1}	critical velocity in approach flow floodplain;

V_{m1}	mean velocity in approach flow main channel;
V_{mc1}	critical velocity in approach flow main channel;
W	abutment setback distance;
x, y, z	streamwise, lateral, and vertical coordinates, respectively;
y_0	unconstricted flow depth in bridge section;
y_1	depth of approach flow;
$y_{2\max}$	maximum water depth at the location of maximum scour;
y_{f0}	unconstricted floodplain flow depth at the bridge section;
y_{f1}	depth of approach flow in floodplain;
$y_{f2\max}$	maximum water depth at the location of maximum scour in the floodplain;
y_{m0}	unconstricted main channel flow depth at the bridge section;
y_{m1}	depth of approach flow in main channel;
$y_{m2\max}$	maximum water depth at the location of maximum scour in the main channel;
κ	von Karman constant;
σ_g	geometric standard deviation of sediment size distribution; and
ν	kinematic viscosity.

REFERENCES

Arneson, L.A., Zevenbergen, L.W., Lagasse, P.F., and Clopper, P.E. (2012). "Evaluating scour at bridges-fifth edition." *Hydraulic Engineering Circular 18* (*HEC-18*), U.S. Federal Highway Administration, Washington, D.C.

Chrisohoides, A., Sotiropoulos, F. and Sturm, T.W. (2003). "Coherent structures in flat-bed abutment flow: Computational fluid dynamics simulations and experiments." *J. Hydraul. Eng.*, 129(3), 177-186.

Ettema, R., Yorozuya, A., Nakato, T., and Muste, M. (2008). "Three abutment scour conditions investigated with laboratory flume." *Proc., 4th Int. Conf. on Scour and Erosion*, Japanese Geotechnical Society, Tokyo.

Ettema, R., Nakato, T., and Muste, M. (2010). "Estimation of scour depth at bridge abutments." *Rep. No. NCHRP 24-20*, National Co-operative Highway Research Program, Washington D.C.

Froehlich, D.C. (1989). "Local scour at bridge abutments." *Proc., National Conference of Hydraulic Engineering*, New Orleans, LA, ASCE, Reston, VA,13-18

Garcia, C.M., Cantero, M. I., Nino, Y., and Garcia, M. H. (2005). "Turbulence measurements with acoustic Doppler velocimeters." *J. Hydraul. Eng.*, 131(12), 1062-1073.

Ge, L., Lee, S., Sotiropoulos, F., and Sturm, T. W. (2005). "3D unsteady RANS modeling of complex hydraulic engineering flows. Part II: Model validation and flow physics." *J. Hydraul. Eng.*, 131(9), 809-820.

Goring, D.G. and Nikora, V.I. (2002). "Despiking acoustic Doppler velocimeter data." *J. Hydraul. Eng.*, 128(1), 117-126.

Guo, J., Kerenyi, K., and Pagan-Ortiz, J.E. (2009). "Bridge pressure flow scour for clear water conditions." *Rep. No. FHWA-HRT-09-04120*, U.S. Federal Highway Administration, McLean, VA.

Hong, S. (2005). “Interaction of bridge contraction scour and pier scour in a laboratory river model.” Master’s thesis, Georgia Institute of Technology, Atlanta, GA.

Hong, S. (2013). “Prediction of clear-water abutment scour depth in compound channel for extreme hydrologic events.” Ph.D. thesis, Georgia Institute of Technology, Atlanta, GA.

Hong, S. and Sturm, T.W. (2009). “Physical model study of bridge abutment and contraction scour under submerged orifice flow conditions.” *Proc., 33rd IAHR Congress: Water Engineering for a Sustainable Environment*, Vancouver, ASCE, Reston, VA.

Hong, S. and Sturm, T.W. (2010). “Physical modeling of abutment scour for overtopping, submerged orifice and free surface flows.” *Proc., 5th Int. Conf. on Scour and Erosion*, San-Francisco.

Hong, Seung Ho, Sturm, T. W., and Stoesser, T. (2015). “Clear-water abutment scour depth in compound channel for extreme hydrologic events,” *J. Hydraul. Eng*., ASCE, 141(6), June 2015.

Koken, M. and Constantinescu, G. (2006). “Investigation of flow around a bridge abutment in a flat bed channel using large eddy simulation.” *Proc., World Environmental and Water Resources Congress* 2006, Omaha, ASCE, Reston, VA.

Koken, M. Constantinescu, G. (2009). “An investigation of the dynamics of coherent structures in a turbulent channel flow with a vertical sidewall obstruction.” *Physics of Fluids*, 21, 085104. doi:10.1063/1.3207859

Lacey, R.W. Jay and Rennie, C.D. (2012). “Laboratory investigation of turbulent flow structure around a bed-mounted cube at multiple flow stages.” *J. Hydraul. Eng.*, 138(1), 71-84.

Lagasse, P.F., Clopper, P.E., Pagan-Ortiz, J.E., Zevenbergen, L.W., Arneson, L.A., Schall, J.D., and Girard, L.G. (2009). “Bridge scour and stream instability countermeasures.” *Hydraulic Engineering Circular 23* (*HEC-23*), U.S. Federal Highway Administration, Washington, D.C.

Laursen, E.M. (1960). “Scour at bridge crossings.” *J. Hydr. Div.,* 86(HY2), 39-54.

Laursen, E. M. (1963). "An analysis of relief bridge scour." *J. Hydr. Div.,* 89(HY3), 93-118.

Lee, Seung Oh, Sturm, T.W., Gotvald, A., and Landers, M. (2004). “Comparison of laboratory and field measurements of bridge pier scour.” *Proc., 2nd Int. Conf. on Scour and Erosion*, Singapore, 231-239.

Lyn, D. (2008). "Pressure-flow scour: A reexamination of the HEC-18 equation." *J. Hydraul. Eng.*, 134(7), 1015-1020.

Melville, B.W. (1992). "Local scour at bridge abutments." *J. Hydraul. Eng.*, 118(4), 615-631.

Paik, J., Sotiropoulos, F. (2005). “Coherent structure dynamics upstream of a long rectangular block at the side of a large aspect ratio channel.” *Phys. Fluids*, 17, 115104.

Richardson, E.V. and Davis, S.R. (2001). “Evaluating scour at bridges-fourth edition.” *Hydraulic Engineering Circular 18* (*HEC-18*), U.S. Federal Highway Administration, Washington, D.C.

Sturm, T.W. and Janjua, N.S. (1994). “ Clear-water scour around abutments in floodplains.” *J. Hydraul. Eng.*, 120(8), 956-972.

Sturm, T.W. (1999). “Abutment scour in compound channels.” *Stream Stability and Scour at Highway Bridges*, E. V. Richardson and P.F. Lagasse, eds., ASCE, Reston, Va., 443-456.

Sturm, T.W. (2006). “ Scour around bankline and setback abutments in compound channels.” *J. Hydraul. Eng.*, 132(1), 21-32.

Sturm. T.W., Ettema, R., and Melville, B.M. (2011). “Evaluation of bridge-scour research: Abutment and contraction scour processes and prediction.” *Rep. No. NCHRP P24-27*, National Co-operative Highway Research Program, Washington, D.C.

Teruzzi A., Ballio F., Armenio V. (2009). “Turbulent stresses at the bottom surface near an abutment: Laboratory-scale numerical experiment.” *J. Hydraul. Eng.*, 135(2), 106–117.

Umbrell, E. R., Young, G. K. Stein, S.M., and Jones J.S. (1998). "Clear-water contraction scour under bridges in pressure flow." *J. Hydraul. Eng.*, 124(2), 236-240.

Voulgaris, G. And Trowbridge, J.H. (1998). “Evaluation of the acoustic Doppler velocimeter (ADV) for turbulence measurements.” *J. Atmos. Ocean. Technol.*, 15, 272-289.

CHAPTER 3

APPLICATION OF CFD MODEL TO BRIDGE OVERTOPPING FLOWS

INTRODUCTION

A submerged bridge, including deck and abutments, is a significant obstacle to the flow creating a backwater effect upstream of the bridge and a distinct and strongly varying water surface profile over the bridge deck and immediately downstream. Most studies in the literature examine experimentally the flow characteristics of free surface flow through the bridge opening including complex 3D coherent structures and scouring mechanisms around abutments (Melville 1995, Oliveto and Hager 2002, and Sturm 2006) and numerically (Biglari and Sturm 1998, Chrisohoides et al. 2003, Paik et al. 2004, Paik and Sotiropoulos 2005, Nagata et al. 2005, Koken and Constantinescu 2008, 2009, 2011, Teruzzi et al., 2009). However, there are only a few studies reported in the literature on flow over inundated bridges and the accompanying water surface profiles. Picek et al. (2007) conducted experiments to derive equations for backwater and discharge for flows through partially or fully-submerged rectangular bridge decks. Malavasi and Guadagnini (2003) carried out experiments to examine the hydrodynamic loading on a bridge deck having a rectangular cross section for different submergence levels and deck Froude numbers. The experimental data was used to analyze the relationship between force coefficients, the deck Froude number and geometrical parameters. They extended their experimental studies to analyze mean force coefficients and vortex shedding frequencies for various flow conditions due to different elevations of the deck above the channel bottom (Malavasi and Guadagnini 2007). Guo et al. (2009) investigated hydrodynamic loading on an inundated bridge and the flow field around it. An experiment was conducted for a six-girder bridge deck model and the experimental data was used to validate complementary numerical simulations. In the experiments, the PIV technique was used to obtain velocity distributions. The numerical data was analyzed for different scaling factors to determine the effects of scaling on hydrodynamic loading. Lee et al. (2010) focused on water surface profiles formed as a result of different bridge structures. They investigated three cases: a cylindrical pier, a deck, and a bridge (i.e. cylindrical pier and deck). Overtopping flow was considered only for the deck and bridge cases. In the experiment, the PIV method was used to measure the velocity. A 3D Reynolds-Averaged Navier Stokes (RANS) model with k-ε turbulence closure was used to simulate all the cases. The volume of fluid method was utilized for free surface modeling. Finally, comparisons of velocity distributions and water surface levels obtained from experiments and simulations showed that the model estimates velocity distributions very well. However, it underestimates the water level rise around the structure due to inability of the k-ε turbulence model to represent such a complex flow having significant streamline curvature and body force effects.

The objectives of this study are to quantify the mean and instantaneous flow through a bridge opening with overtopping, to elucidate the complex three-dimensional hydrodynamics and discuss their potential effects on the local scour mechanism. As seen in the previous chapter, the generation of turbulent kinetic energy by flow separation around the abutment and the horseshow vortex system can be correlated with the scour that occurs there. *The purpose herein is to demonstrate by computation fluid dynamics (CFD) a more detailed view of the complex turbulent processes driving scour than can be measured in the laboratory. Of primary importance in simulating the turbulence is to capture accurately the free-surface position as the flow accelerates through and over the bridge in the case of overtopping.* With this in mind, an existing, state-of-the-art large-eddy simulation (LES) approach is refined with a level-set method applied in the free surface algorithm which provides unprecedented details of the water surface deformation and turbulence characteristics. The simulations are complemented with an analogous laboratory experiment, and the data are used to validate the LES.

The material in this chapter is derived from the Ph.D. thesis of Kara (2014) and the article by Kara et al. (2015). The reader may consult these sources for more details.

NUMERICAL MODELING BACKGROUND

The concept of numerical modeling of fluid flows, or Computational Fluid Dynamics (CFD), is not new, but its capabilities have advanced rapidly in recent years due to the development of ever faster computer processors placed in parallel. Numerical modeling begins with the basic differential equations of fluid motion (mass conservation or continuity, and momentum conservation or Navier-Stokes equations), and transforms them into algebraic equations that are valid on specified spatial grids overlaid on the flow domain. The size of the grid spacing is very important with respect to accuracy and convergence of the numerical algorithms utilized in the approximation and solution of the governing equations. Specification of appropriate boundary conditions is an essential step in the development of a numerical model. Finally, validation of the model in comparison with analytical solutions and experimental data is necessary to establish its accuracy and applicability to the problem at hand.

The effective representation of turbulence is the key feature of CFD models in hydraulic engineering, and its role in the scour process is especially relevant in the context of this project. While increased energy dissipation caused by turbulence at the boundary of shear flows such as in pipes or open channels is well known (Munson et al. 2013), its contribution to enhanced mixing and transport of sediment is a subject of continuing research (Lyn 2008). One of the confounding aspects of turbulence with respect to CFD models is that its properties include a wide range in the physical size of eddies, from large-scale eddies that depend on the geometry of the flow domain to the smallest sizes at which energy dissipation occurs. Because the ratio of large-scale to small-scale eddy sizes increases with increasing Reynolds number, modeling high Reynolds number turbulent flows in hydraulic engineering becomes particularly challenging. Mesh sizes small enough to capture the behavior of all eddy sizes through direct numerical simulation (DNS) literally becomes impossible even with today's computing power (Rodi et al. 2013).

Reynolds-averaged Navier-Stokes (RANS) equation approaches depend on averaging the Navier-Stokes equations in time, and solving for the mean flow quantities. In the process of averaging the convective terms (flow acceleration terms), interactions between the turbulent fluctuations appear that are treated as turbulent or Reynolds stresses. The turbulence closure problem then becomes evaluating the Reynolds stresses with a whole range of turbulence submodels available (Rodi 1993). The RANS CFD models, however, cannot capture the large-scale unsteadiness and energetics of coherent eddies associated with the horseshoe vortex involved in local scour. Here the term "coherent" refers to an irregular, identifiable pattern of eddies superimposed on the random fluctuations engendered by the smaller-scale eddies. For problems such as local scour that include unsteady, large-scale eddies, the large-eddy simulation (LES) technique is more suitable as discussed in detail by Rodi et al. (2013).

In this chapter, the initial validation of HYDRO3D, which is an LES model, is discussed briefly to illustrate its capabilities in the complex flow situations associated with submerged orifice and bridge overtopping flow in this project. Of special interest is demonstration of the turbulent kinetic energy (TKE) generation in bridge overtopping flows and its spatial distribution because of its connection to scouring of the sediment bed. Further validation of the model will be based on experimental results from the Georgia Tech flume in future research.

NUMERICAL FRAMEWORK

In this study, the governing equations for an unsteady, incompressible, viscous flow of a Newtonian fluid are solved using the in-house code HYDRO3D (Stoesser and Nikora 2008, Stoesser 2010, Bomminayuni and Stoesser 2011). An LES approach is employed to simulate directly the large, energy carrying eddies while scales smaller than the grid size are accounted for using the WALE subgrid scale model (Nicoud and Ducros 1999). The code is a refined and improved version of the open-channel LES code that was validated for flow over dunes (Stoesser et al. 2008), flow in compound channels (Kara et al. 2012) and flow in contact tanks (Kim et al. 2010, 2013). HYDRO3D is based on finite differences with staggered storage of the Cartesian velocity components on uniform Cartesian grids. Second-order central differences are employed for the diffusive terms while convective fluxes in the momentum and level-set equations (see below) are approximated using a fifth-order weighted essentially non-oscillatory (WENO) scheme. The WENO scheme offers the necessary compromise between numerical accuracy and algorithm stability (especially important for the free-surface algorithm, see below). A fractional-step method is used with a Runge-Kutta predictor and the solution of a pressure-correction equation in the final step as a corrector. A multi-grid method is employed to solve the Poisson equation. The code is parallelized via domain decomposition, and the standard Message Passing Interface (MPI) accomplishes communication between sub-domains.

The major refinement of the code is the treatment of the free water surface for which a new algorithm has been implemented. It is based on the level set method (LSM) developed by

Osher and Sethian (1988), which is an interface-capturing method for a two-phase (water and air) flow performed on a fixed grid. The LSM employs a level set signed distance function, ϕ, which has zero value at the phase interface and is negative in air and positive in water. This method is formulated as:

$$\phi(x,t)\begin{cases} < 0 \quad if \quad x \in \Omega_{gas} \\ = 0 \quad if \quad x \in \Gamma \\ > 0 \quad if \quad x \in \Omega_{liquid} \end{cases} \tag{3.1}$$

where Ω_{gas} and Ω_{liquid} represent the fluid domains for gas and liquid, respectively, and Γ is the interface. The interface moves with the fluid particles, expressed through a pure advection equation of the form (Sethian and Smereka 2003):

$$\frac{\partial \phi}{\partial t} + u_i \frac{\partial \phi}{\partial x_i} = 0 \tag{3.2}$$

Validation of the free-surface algorithm in the code was accomplished by application to the problem of propagation of a solitary wave in a rectangular channel and its run-up on a vertical wall. The CFD model produced a solitary wave speed within 5% of the theoretical value. Comparisons with wave run-up values, both measured and computed by other investigators, showed excellent agreement. Details can be found in Kara (2014) and Kara et al. (2015).

EXPERIMENTAL AND COMPUTATIONAL SETUP

The computational setup shown in Fig. 3.1 was chosen to correspond to the complementary physical experiments carried out in Cardiff University's hydraulics laboratory. A 10m long, *W*=0.30m wide tilting flume (bed slope 1/2000) was equipped with a model bridge consisting of

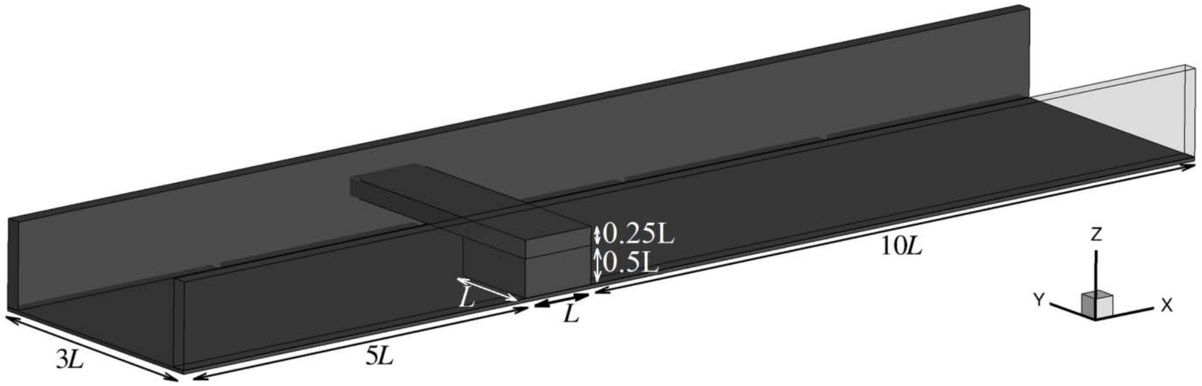

Figure 3.1. Computational setup. (Kara 2014).

a square abutment with length and width of L=0.1m, and height of h_a=0.05m. The rectangular bridge deck had a girder thickness of h_d=0.024m, and it extended across the channel. The model bridge is an idealized version of the Towaliga River Bridge near Macon, Georgia. The geometric contraction ratio of bridge opening width to channel width was 0.67. In the simulation the deck thickness was taken as h_d=0.025m which allowed for more efficient grid generation and code parallelization. Before inserting the bridge model into the flume, the stage-discharge relationship for uniform flow was established and the flow depth was controlled via a weir at the downstream end. With the bridge in place, the water backed up and caused an increase of water depth upstream of the bridge. The discharge, chosen as Q=8.5l/s corresponds to an extreme flood event for which the uniform flow depth was H=9.2cm. This resulted in a bulk velocity of U_b=0.3m/s and a mean shear velocity of u_*=0.017m/s. The Reynolds number based on U_b and four times the hydraulic radius, was R = 70,250, and the Froude number of the uniform flow was F = 0.32. In the experiment, detailed water surface profiles were measured using a point gage. The laboratory and numerical setups are presented in Fig. 3.1, in which all dimensions are normalized with the length/width of the abutment, L.

In the LES, a constant discharge is introduced into the system at the inlet section, a simplified inlet treatment, which is necessary due to the fact that the water surface elevation is unknown initially at the inlet. The convective boundary condition is used at the outlet ensuring that coherent structures leave the system without creating unphysical numerical oscillations that reflect into the domain. The no-slip boundary condition is employed for all walls including the bridge abutment and deck. The computational domain is discretized with a uniform mesh and several resolutions are tested. The flow is driven by gravity, $g=9.81\ m/s^2$ and the dynamic viscosity and density of water (air) are 1×10^{-3} (1.8075×10^{-5})kg/(m-s) and 1000(1.205)kg/m^3, respectively; hence, Reynolds number, R, and Froude number, F, of the simulation are the same as in the experiment. The simulation is run initially for a period of 10 eddy turn-over times ($t_e = H/u_*$) to develop the flow and establish the correct water surface elevation, and is then continued for another $51t_e$ to obtain turbulence statistics.

RESULTS AND DISCUSSION

Fig. 3.2 (top) presents an overall three-dimensional view of the time-averaged water surface of this flow as predicted by the numerical simulation. Also plotted (bottom right) is a close-up photograph of the corresponding flow over the bridge in the experiment. The flow accelerates over the bridge, which results in a marked drop of the water surface. The flow plunges downstream of the bridge, which results in a standing wave or an undular hydraulic jump. Downstream of the standing wave the flow recovers gradually, exhibiting wavy motion, to the uniform flow condition. In general, Fig. 3.2 shows very good qualitative agreement between the numerical results and the conditions observed in the laboratory experiment.

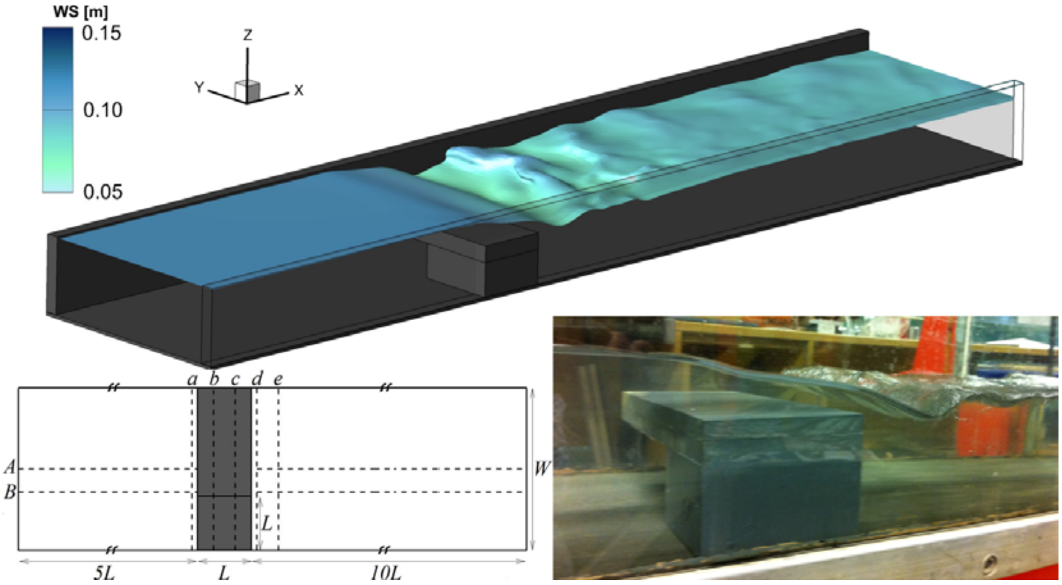

Figure 3.2. Simulated water surface (top), measurement locations (bottom left) and close-up photograph of the laboratory experiment (bottom right). (Kara 2014).

A more quantitative assessment of the predictive capabilities of the simulation results is provided in Figs. 3.3 and 3.4, which depict measured (dots) and simulated (lines) longitudinal (Fig. 3.3) and cross-sectional profiles (Fig. 3.4) of the water surface. The simulated longitudinal profiles (Fig. 3.3) along A and B (see sketch in the lower left of Fig. 3.2) are in very good agreement with the observed data irrespective of grid resolution (blue line = fine grid, black line = coarse grid). There is a small, but consistent overestimation of the water surface elevation on and upstream of the bridge. The reason for this discrepancy is that the height of the bridge deck in the simulation was chosen to be exactly 50% of the depth of water underneath the deck so that the numerical domain was easier to decompose in the vertical, which improved the parallelization of the code. The height of the bridge deck in the experiment was 48% of the depth of water underneath it. There is some discrepancy between numerical prediction and measurement in the vicinity of the standing wave, an area that is highly turbulent and where accurate water surface measurements using a point-gage are difficult to achieve. Fig. 3.4 presents measured and simulated cross-sectional water surface profiles at selected locations (a-e, see Fig. 3.2). Upstream and on the bridge (Profiles a and b) the numerically predicted profiles are slightly higher than the measured ones, whereas numerically predicted Profiles c, d and e are in very good agreement with the measurements.

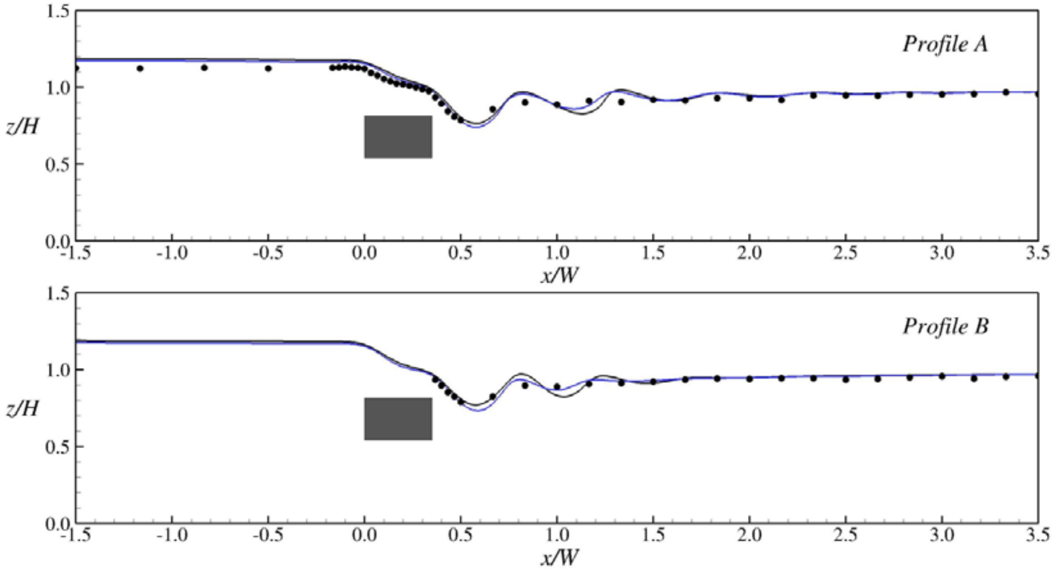

Figure 3.3. Longitudinal water surface profiles along two locations, which are channel center line (Profile A) and one-third of the channel width (Profile B) at the abutment face (Kara 2014).

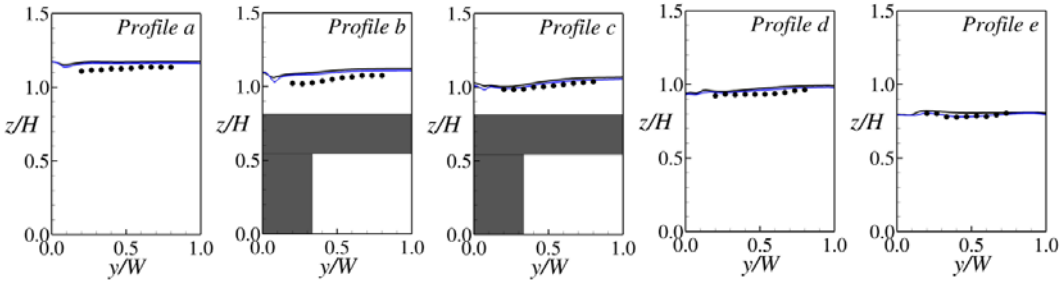

Figure 3.4. Cross-stream water surface profiles along six locations (Profiles a-e) looking upstream (Kara 2014).

Figure 3.5 provides a three-dimensional view of the time-averaged flow, depicting streamlines color coded by the turbulent kinetic energy (*tke*). Fig. 3.5a) provides an oblique view from upstream visualizing the plunging flow over the deck and two distinct vortices (marked as

AV and SV1). The approach flow on the abutment side is forced over the structure in a helical arch-shaped vortex (AV). This vortex rotates counter-clockwise and the rotation is induced near the bed (see Fig. 3.5b) through the abutment-caused separation vortex (SV2a). As the vortex arches over the deck the flow is accelerated and the rotation disappears. The flow separates from the trailing edge of the deck creating a long longitudinal recirculation vortex (denoted SV1 in Fig. 3.5a) downstream of the deck. Near the bed, small separation vortices (SV2a, b and d in Fig. 3.5b) occur around the abutment. The near-bed recirculation zone denoted SV2c is the most significant one, as it generates and carries a significant amount of turbulent kinetic energy. A strong shear layer forms at the interface between this zone and the fast orifice flow from underneath the bridge, in addition the flow from over the deck plunges into this area creating strong turbulence. The *tke* in this shear layer exceeds eighty times the squared shear velocity of the uniform channel flow (u_*^2).

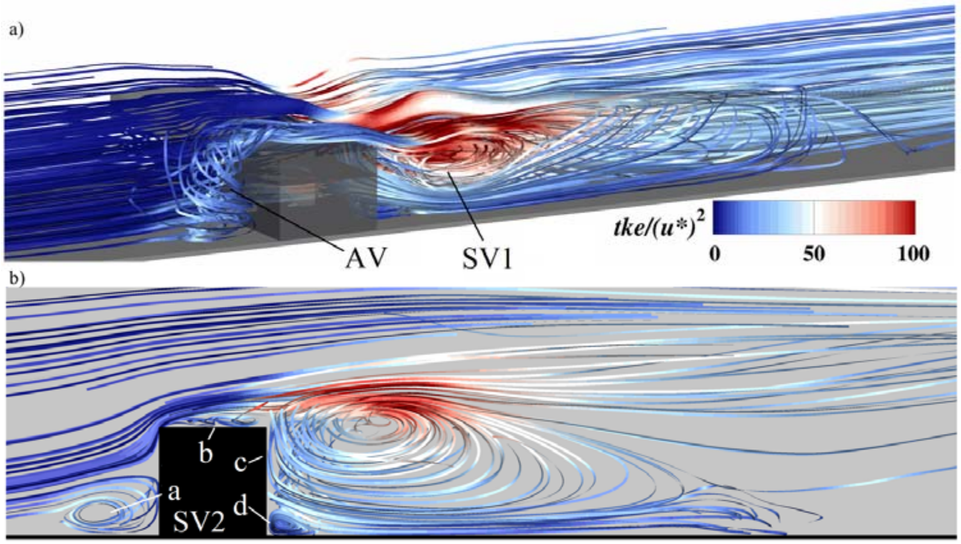

Figure 3.5. Streamlines of the time-averaged flow over a submerged bridge. a) oblique view from behind and b) in a horizontal plane near the bed (Kara 2014).

A more quantitative view of the flow is provided with the help of Fig. 3.6, in which the time-averaged streamwise velocity together with streamlines in three longitudinal planes are plotted. The time-averaged flow over the bridge is subdivided into two portions: 74.8% of the discharge is forced underneath the bridge deck as submerged orifice flow, whilst the remaining 25.2% discharges over the deck as a weir flow. The deck acts similarly to a broad-crested weir and the critical depth of the portion over the deck is $y_c=(q^2/g)^{1/3}$=1.73cm, which is attained at 0.93L, i.e. very close to the trailing edge of the deck. The flow plunges into the downstream area as supercritical flow, and undergoes an "undular" hydraulic jump. A vertical recirculation zone forms downstream of the abutment as depicted in Fig. 3.6a. On the side of the abutment the standing wave is not as steep as in the middle of the channel, a feature that was also observed in the experiment. At y/W=0.33 the separation vortex over the deck interacts with the lateral flow separation and recirculation from the abutment generating a vortex core at x/W=0.7 and a saddle point underneath (Fig. 3.6b). At y/W=0.67 (Figure 3.6c) the submerged orifice flow features streamwise velocities up to almost three times the bulk velocity, which is due to the lateral and vertical contraction of the flow not only by the abutment and deck but also by the vertical and horizontal recirculation zones of the separated flow (see separation vortices SV1 and SV2 in Fig. 3.5).

Fig. 3.7 quantifies the complex flow over the submerged bridge in terms of bed shear stress τ, normalized with the mean boundary shear stress ($<\tau>=\rho gRS$) for uniform flow, and *tke*, normalized with the squared mean shear velocity for uniform flow, u_*^2. The highest values of bed shear stress are observed in the bridge cross-sections and close to the leading edge of the abutment, which is where the flow is contracted. There is also a region of high bed shear slightly downstream of the abutment. The area of highest near-bed *tke* does not coincide with the area of

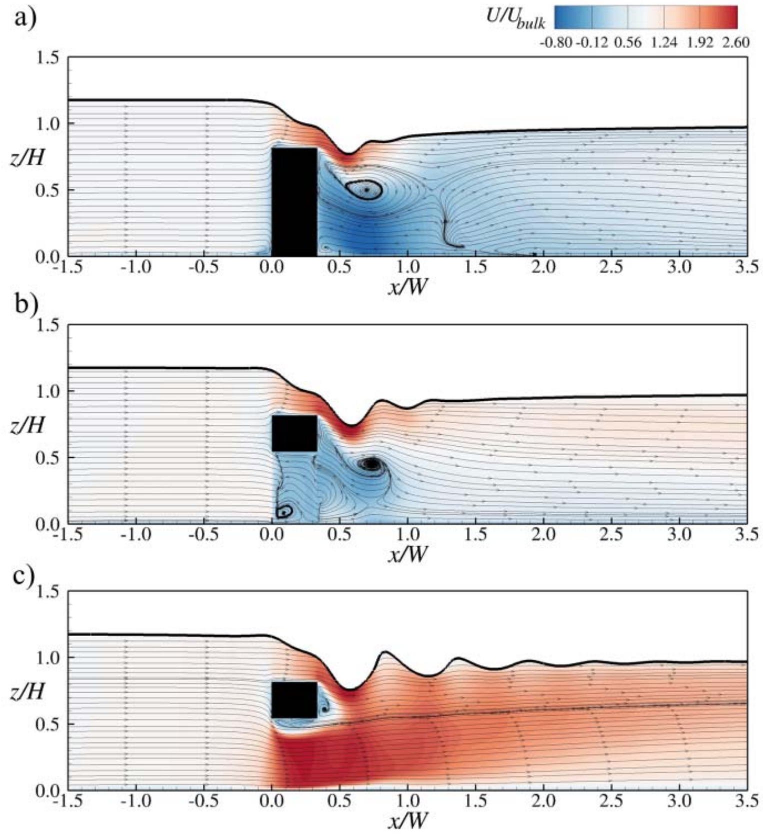

Figure 3.6. Time-averaged velocity contours together with streamlines of the flow in three selected longitudinal-sections: a) *y/W*=0.17; b) *y/W*=0.33; c) *y/W*=0.67 (Kara 2014).

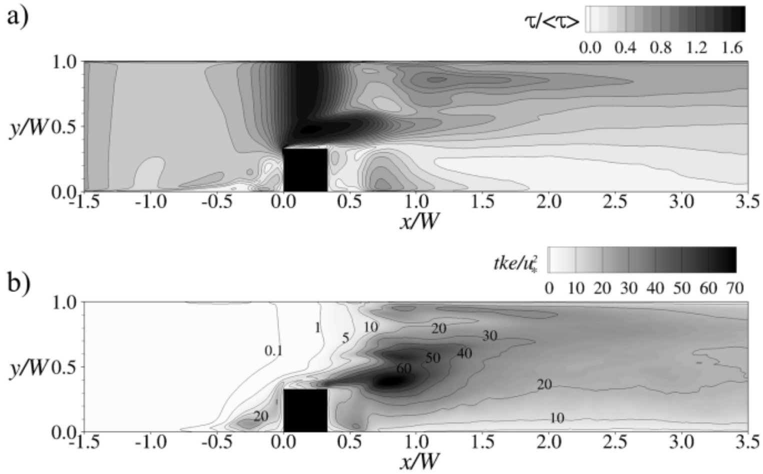

Figure 3.7. a) Contours of the normalized bed-shear stress and b) contours of the normalized turbulent kinetic energy in a horizontal plane at z^+=50. (Kara 2014)

highest bed shear, but as discussed earlier is found where the plunging flow from over the deck coincides with the edge of the lateral recirculation zone of the separated flow.

Fig. 3.8 provides an overview of the many instantaneous turbulence structures and features of this flow. The figure presents instantaneous streamlines in an oblique view from upstream. The afore-mentioned helical arch-vortex is visible as well as the flow acceleration and plunging flow downstream of the deck. The longitudinal recirculation downstream of the deck is not very clear because the flow is too turbulent to identify distinct large-scale vortices. The streamlines are color coded by the instantaneous streamwise velocity, *u*, and areas of fast moving fluid over the deck are discerned as well as areas of negative velocity near the bed behind and in front of the abutment.

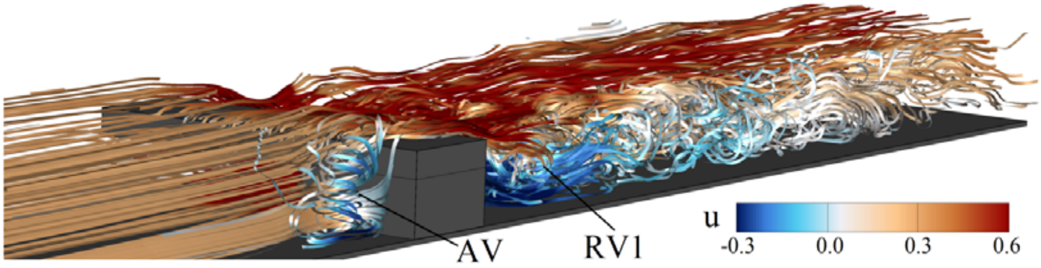

Figure 3.8. Streamlines of the instantaneous flow colored by the instantaneous streamwise velocity. (Kara 2014).

SUMMARY

The flow through a submerged bridge with overtopping was investigated by means of a complementary experimental/numerical study. An idealized bridge model was placed in a flume and detailed water level measurements were used to validate a refined in-house large-eddy simulation (LES) code. A sophisticated numerical approach was chosen for this flow situation because of the complex turbulent structures and the severe water surface curvature caused by the bridge overtopping and lateral flow contraction due to the abutment. Analysis of the LES data revealed the complex nature of the flow featuring various vortical structures around the bridge that were characterized by the turbulent kinetic energy (TKE). In qualitative comparisons with the experimental TKE measurements summarized in Chapter 2, it appears that TKE is an important driving factor that influences the degree of bridge abutment scour.

LIST OF SYMBOLS

F = Froude number (-)

g = acceleration due to gravity (m/s^2)

H = uniform flow depth (m)

h_a = abutment height (m)

h_d = bridge deck girder thickness (m)

L = length and width of the abutment (m)

Q = flow discharge (l/s)

R = hydraulic radius (m)

R = Reynolds number (-)

t = time (s)

t_a = artificial time step for level set re-initialization

t_e = eddy turn-over time (s)

T = non-dimensional time (-)

u = instantaneous streamwise velocity (m/s)

u_i = velocity vector (m/s)

u_* = global shear velocity (m/s)

U_b = bulk velocity (m/s)

W = flume width (m)

x_i = spatial location vector

y_c = critical depth (m)

τ, $<\tau>$ = local, and mean shear stress (N/m^2)

Ω_{gas}, Ω_{liquid} = fluid domains for gas and liquid, respectively

$\phi(x,t)$ = level set function

Γ = interface

ρ_g, ρ_l = density for gas and liquid, respectively (kg/m^3)

μ_g, μ_l = dynamic viscosity for gas and liquid, respectively (kg/(ms))

REFERENCES

Biglari, B., Sturm, T. W. (1998). Numerical modeling of flow around bridge abutments in compound channel. *J. Hydr. Eng.*, *ASCE*, 124(2), 156-164.

Bomminayuni, S., Stoesser, T. (2011). Turbulence statistics in an open-channel flow over a rough bed. *J. Hydr. Eng.*, Vol. 137 (11), pp. 1347-1358.

Chrisohoides, A., Sotiropoulos, F., Sturm, T. W. (2003). Coherent structures in flat-bed abutment flow: computational fluid dynamics simulations and experiments. *J. Hydr. Eng.*, *ASCE*, 129(3), 177-186.

Guo, J., Zhang, T. C., Admiraal, D. M, Bushra, A. (2009). Computational design tool for bridge hydrodynamic loading in inundated flows of Midwest Rivers. Report # *MATC-UNL*:227.

Kara, S. (2014). “Numerical simulation of flow in open-channels with hydraulic structures,” Ph.D. thesis, Georgia Institute of Technology, Atlanta, GA.

Kara, S., Stoesser, T., Sturm, T.W. (2012). Turbulence statistics in compound channels with deep and shallow overbank flows. *J. Hydr. Research*, 50(5), pp 482-493.

Kara, Sibel, Stoesser, Thorsten, Sturm, Terry W., and Saad, Mulahasan. “Flow dynamics through a submerged bridge opening with overtopping,” *J. Hydr. Research*, 53(2), 186-195, 2015.

Kim, D., Kim, D., Kim, J.H., Stoesser, T. (2010). Large eddy simulation of flow and solute transport in ozone contact chambers. *ASCE J. Environ. Eng.,* Vol. 136 (1), pp 22-31.

Kim, D., Kim, J.H., Stoesser, T. (2013). Hydrodynamics, turbulence and solute transport in ozone contact chambers. *IAHR J. Hydr. Res.* Vol**.** 51(5), 558-568.

Koken, M., Constantinescu, G. (2008). An investigation of the flow and scour mechanisms around isolated spur dikes in a shallow open channel. Part I. Conditions corresponding to the initiation of the erosion and deposition process. *Water Resources Research*, 44, W08406, DOI:10.1029/2007WR006489.

Koken, M., Constantinescu, G. (2009). An investigation of the dynamics of coherent structures in a turbulent channel flow with a vertical sidewall obstruction. *Physics of Fluids*, 21, 085104, DOI 10.1063/1.3207859.

Koken, M., Constantinescu, G. (2011). Flow and turbulence structure around a spur dike in a channel with a large scour hole. *Water Resources Research*, 47, W12511, doi:10.1029/2011WR010710.

Lee, D., Nakagawa, H., Kawaike, K., Baba, Y., Zhang, H. (2010). Inundation flow considering overflow due to water level rise by river structures. *Annuals of Disas. Prev. Res. Inst.*, Kyoto Univ., No. 53 B.

Lyn, D. (2008). "Turbulence models in sediment transport engineering," Chapter 16 in Sedimentation engineering: measurements, modeling, and practice, edited by M. Garcia, ASCE Manual of Practice No. 110, ASCE, Reston, VA.

Malavasi, S., Guadagnini, A. (2003). Hydrodynamic loading on river bridges. *J. Hydr. Eng.*, ASCE, 129 (11), 854-861.

Malavasi, S., Guadagnini, A. (2007). Interactions between a rectangular cylinder and a free-surface flow. *Journal of Fluids and Structure*, 23, 1137–1148.

Melville, B. W. (1995). Bridge abutment scour in compound channels. *J. Hydr. Eng.*, ASCE, 121 (12), 863-868.

Munson, B., Rothmayer, A., Okiishi, T., and Huebsch, W. (2013). *Fundamentals of fluid mechanics,* 7th edition, John Wiley & Sons, New York.

Nagata, N., Hosoda, T., Nakato, T., Muramoto, Y. (2005). Three-dimensional numerical model for flow and bed deformation around river hydraulic structures. *J. Hydr. Eng.,* 131(12), 1074-1087.

Nicoud, F., Ducros, F., (1999). Subgrid-scale stress modelling based on the square of the velocity gradient tensor. *Flow Turbul Combust* 62, 183-200.

Oliveto, G., Hager, W. H. (2002). Temporal evolution of clear-water pier and abutment scour. *J. Hydr. Eng.*, ASCE, 128(9), 811-820.

Osher, S., Sethian, J.A. (1988). Fronts propagating with curvature-dependent speed algorithms based on Hamilton-Jacobi formulations. *Journal of Computational Physics* 79(1), 12-49.

Paik, J., Ge, L., Sotiropoulos, F. (2004). Toward the simulation of complex 3D shear flows using unsteady statistical turbulence models. *Int. J. of Heat and Fluid Flow*, 25, 513-527.

Paik, J., Sotiropoulos, F. (2005). Coherent structure dynamics upstream of a long rectangular block at the side of a large aspect ratio channel. *Physics of fluids* 17, 115104.

Picek, T., Havlik, A., Mattas, D., Mares, K. (2007). Hydraulic calculation of bridges at high water stages. *J. Hydr. Research*, 45, pp. 400-406.

Rodi, W. (1993). Turbulence Models and their Application in Hydraulics. 3rd edition. IAHR Monograph, Rotterdam: A.A. Balkema.

Rodi, W., Constantinescu, G., Stoesser, T. (2013). *Large Eddy Simulation in hydraulics*. *IAHR Monograph*, CRC Press, Taylor & Francis Group (ISBN-10: 1138000247).

Sethian, J. A., Smereka, P. (2003). Level set methods for fluid interfaces. *Annu. Rev. Fluid Mech.*, 35, 341-372.

Stoesser, T., Braun, C., Garcia-Villalba, M. , Rodi W. (2008). Turbulence Structures in Flow over Two Dimensional Dunes. *ASCE, J. Hydr. Eng.*, Vol. 134 (1), pp. 42-55.

Stoesser, T., Nikora, V. (2008). Flow structure over square bars at intermediate submergence: Large Eddy Simulation (LES) study of bar spacing effect. *Acta Geophysica*, Vol. 56, No. 3, pp. 876-893.

Stoesser, T. (2010). Physically realistic roughness closure scheme to simulate turbulent channel flow over rough beds within the framework of LES. *J. Hydr. Eng.*, Vol. 136 (10), pp. 812-819.

Sturm, T. W. (2006). Scour around bankline and setback abutments in compound channels. *J. Hydr. Eng.*, ASCE, 132 (1), 21-32.

Teruzzi A., Ballio F., Armenio V. (2009). Turbulent stresses at the bottom surface near an abutment: Laboratory-scale numerical experiment. *J. Hydr. Eng.*, 135(2), 106–117.

CHAPTER 4

EFFECTS OF PHYSICAL PROPERTIES ON EROSIONAL AND YIELD STRENGTHS OF FINE-GRAINED SEDIMENTS

INTRODUCTION

Erosional resistance of sediments compared to hydrodynamic forces that cause scour processes described in Chapters 2 and 3 of this report are equally important in the final determination of expected scour depths and the safety of bridge foundations. While prediction of erosional resistance of coarse-grained sediments is well known, erodibility and transport mechanisms for fine-grained sediments (silt and clay) are quite different because of the mineral structure of clay particles which are "cohesive" due to electrostatic and molecular forces that bind them.

Erodibility of sediment as defined herein in terms of the critical value of hydrodynamic shear stress (τ_c) required to overcome interparticle forces in cohesive sediments and initiate particle movement. The mode of erosion can be floc erosion, surface erosion, or mass erosion (Winterwerp et al. 2012, Mehta and McAnally 2008). Winterwerp et al. (2012) suggested that floc erosion occurs when some of the instantaneous turbulent fluctuations of the bed shear stress exceed τ_c, while surface erosion involves continuous removal and entrainment of surface layers of flocs. Mass erosion, on the other hand, is an undrained bulk shear failure, in the soil mechanics sense, of a large section of bed accompanied by washing away of large chunks of sediment at very high erosion rates. If erosion that occurs for bed shear stresses smaller than τ_c is assumed negligible (Karmaker and Dutta 2011; Osman and Thorne 1988), then critical shear stress can be defined for experimental purposes as the mean bed shear stress at which erosion just begins.

Although progress has been made in recent years, the capability to predict erodibility of fine, cohesive sediment beds is still in question (Grabowski et al. 2011). Previous research has focused on developing empirical relationships for erodibility of sand-mud (silt and clay) mixtures collected from the field or made by artificial mixing in the laboratory (e.g. Ternat et al. 2008; Debnath et al. 2007; van Ledden et al. 2004; Reddi and Bonala 1997; Mitchener and Torfs 1996). Most studies have lumped silt and clay together as "mud" (or fines) in the sediment mixture, and a few studies have focused on characterizing the erosional characteristics and their determining factors for clay-sized sediments alone (e.g. Ravisangar et al. 2005; 2001). While it is important to note that it is actually the clay particles within the fine sediment fraction which provide cohesive properties (van Ledden et al. 2004), there has been little effort to study cohesive effects of clays in combination with silts relative to sediment erosion. The nature of clay and silt is different in terms of mineralogy, water-holding capacity, and electrochemistry at the particle surface due to their differences in particle size (Santamarina 2001). Clay content should be distinguished from silt in fine sediments and considered as one of the key factors influencing fine sediment erodibility.

Some investigators have suggested that rheology, which is the science describing the rate of deformation or flow of a material subjected to applied stresses as determined by the particle microstructure, can be applied to the problem of determining the erodibility of fine-grained sediments. For hyperconcentrations such as fluid muds, rheological properties indicate how the sediment matrix responds under a hydrodynamic shear stress induced by a river flow, for example. One of the rheological characteristics of sediments is the yield stress (τ_y), defined as the limiting value of shear stress required for the sediment to begin to flow (Dade et al. 1992; Nguyen and Boger 1992). Otsubo and Muraoka (1988) and Ravisangar et al. (2001) studied the rheological and erosion behavior of natural muds and pure kaolinite, respectively, and both studies found positive correlations between rheological properties and erosion thresholds for fine sediments.

In previous studies conducted by Navarro (2004) and Hobson (2008) at the Georgia Institute of Technology, Shelby tube sediment samples were collected from river bed sediments near bridge foundations around the state of Georgia. As summarized by Hobson et al. (2010), they measured critical shear stress, τ_c, of the samples in an erosion flume and yield stress, τ_y, with a rheometer as described herein for the present study. Their results indicated a strong correlation of dimensionless forms of τ_c and τ_y with independent variables describing the sediment properties of the field samples for both fine and coarse-grained sediments.

This study aims to (1) determine experimentally how the erosional and yield strengths of fine sediments depend on sediment physical properties; and (2) identify and quantify relationships among dimensionless forms of erosional strength (Shields' parameter), yield strength (dimensionless yield stress), and the physical properties of fine sediments to solve the engineering problem of bridge foundation scour (e.g. Sturm 2006; Lee and Sturm 2009). This chapter of the report is based on the Ph.D. thesis of Wang (2013) and further details can be found there.

EXPERIMENTAL MATERIALS AND METHODS

Sample Preparation

In this study, industrial-grade Georgia kaolin (kaolinite) and ground silica were used as the sediment materials to prepare sediment mixtures. Georgia kaolin, obtained from Imerys USA, Inc. of Roswell, Georgia (formerly Dry Branch Kaolin Company, Dry Branch, Georgia), is graded as Hydrite Flat D in the industry. Industrial ground silica (SIL-COSIL 106) from Ottawa, Illinois, was purchased from U.S. Silica Company. Typical physical properties of the sediments are shown in Table 4.1.

Table 4.1. Typical physical properties of Georgia kaolin and industrial ground silica (Wang 2013).

Property **Georgia Kaolin**	**Value**
Median particle size (d_{50}) from the hydrometer test	2.6μm (by weight)
Median particle size (d_{50}) by a Brinkman particle size analyzer [a]	0.95μm (by number count)
Mean particle size by a Brinkman particle size analyzer [a]	1.5μm (by number count)
pH of 20% aqueous slurry	4.2~5.2
BET (N_2 adsorption) specific surface	10.5~10.9 m^2/g
Methylene blue adsorption [b] specific surface	10.5~11.2 m^2/g
Specific gravity	2.58
Property **Industrial ground silica (SIL-COSIL 106)**	
Median particle size (d_{50})	32μm (by weight)
Hardness (Mohs)	7
Mineral	Quartz
pH	7
Specific gravity	2.65

Note: [a] Value reported in Ravisangar et al. (2005)
[b] Conducted by following the procedure suggested in Santamarina et al. (2002)

Sediment mixtures were prepared from the mixed sediments consisting of different proportions of ground silica and Georgia kaolin by dry weight. Specifically, sediment mixtures with 10%, 20%, 40%, 60%, and 100% kaolin contents were prepared by mixing 450 g of air-dry sediments with 720 ml of tap water using an electronic blender; the initial mass concentrations of the slurry were approximately 505 g/l. Then the sediment suspension was poured into the coring container, which was a cut-off section of a Shelby tube with an inner diameter of 73 mm and a height of 294 mm, in which an alloy piston was inserted as the bottom. The suspension was allowed to settle naturally for 24 hours; a longer settling time of 48 hours produced essentially no change in the height of the settled column in confirmation of the experiments of Ravisangar et al. (2005). After 24 hours of settling, the consolidation ranged from 10% to 54% in volume, and 88 ml to 489 ml excess water was suctioned off the top with as little disturbance as possible before running flume experiments or rheometer tests.

Sediment Property Tests

Conventional geotechnical tests including water (moisture) content, dry and bulk densities, and grain size distribution were carried out for each layer of the sediment mixtures consisting of different kaolin proportions. Each specimen was prepared separately for these tests and sectioned into three to four layers. The water content was measured for each layer to obtain the bulk density as a function of sediment depth. Layers of sediments sectioned from one specimen were labeled as top, middle(1), middle(2), and bottom, indicating the locations of sediment layers in the whole specimen. In addition, temperature, pH value, and conductivity of tap water and the sediment slurry of each specimen were measured and recorded.

The water content in each specimen was determined by following the procedure outlined in ASTM D 2216-05, which defines the water content as the ratio of pore water mass to the mass of dry solids. The dry and bulk densities were estimated from the measured water content by assuming all the specimens were 100% saturated such that the pore spaces between particles were filled with water and negligible air. Grain size distributions of the ground silica, Georgia kaolin, and silt-clay mixtures were determined by sieve analysis and hydrometer tests. The tests were carried out in accordance with ASTM C136-01, ASTM D1140-00, and ASTM D 422-63-02 for dry sieve analyses, wet sieve analyses, and hydrometer tests, respectively. The plasticity index values for different sediment mixtures were measured based on the ASTM D 4318-10 protocol.

The temperature, pH value, and conductivity of the tap water and sediment mixtures were measured by an Oakton waterproof PC 300 hand-held meter, which compensates the temperature effects automatically when the conductivity electrode with a built-in temperature sensor is plugged in. While the temperature calibration was provided by the manufacturer, calibrations of pH and conductivity were performed using standard calibration buffers before taking measurements.

Hydraulic Flume Experiments

The flume experiments were conducted in a recirculating, rectangular, tilting flume located in the hydraulics laboratory at the Georgia Institute of Technology as shown in Fig. 4.1. The flume dimensions are 6.1 m in length, 0.38 m in width, and 0.38 m in depth. The fixed gravel bed of the flume with d_{50} = 3.3 mm ensured a fully-rough ($\frac{u_* k_s}{\nu} \geq 70$; $k_s = 1.67 d_{50}$) turbulent flow condition around the specimen during the flume erosion test. The Shelby tube was inserted through the bottom of the flume and sealed with a rubber O-ring at a location 4.3 m downstream of the flume entrance which provided a fully-developed boundary layer. No influences of change in bed roughness on the bed shear stress could be discerned over the short length of the sample at the centerline of the flume as justified previously by Ravisangar et al. (2005).

The recirculating flow to the flume was provided from a 1.9 m^3 storage tank using a variable-speed slurry pump that can pass large solids. A desired bed shear stress (τ) for the flume erosion test was produced by an operator-controlled flow rate, a tailgate to set the uniform flow depth, and channel bed slope. To measure the flow rate and the channel slope, a bend meter and a slope counter, respectively, were calibrated by previous researchers (Hoepner 2001; Ravisangar et al. 2001). Design of the hydraulic flume and determination of flow conditions are detailed in Ravisangar et al. (2005), Hobson (2008), and Wang (2013). Shear stresses between approximately 1 Pa and 21 Pa can be achieved. The experimental procedures used in this research followed those in the studies of Hobson (2008), Navarro (2004), Hoepner (2001), and Ravisangar et al. (2005; 2001).

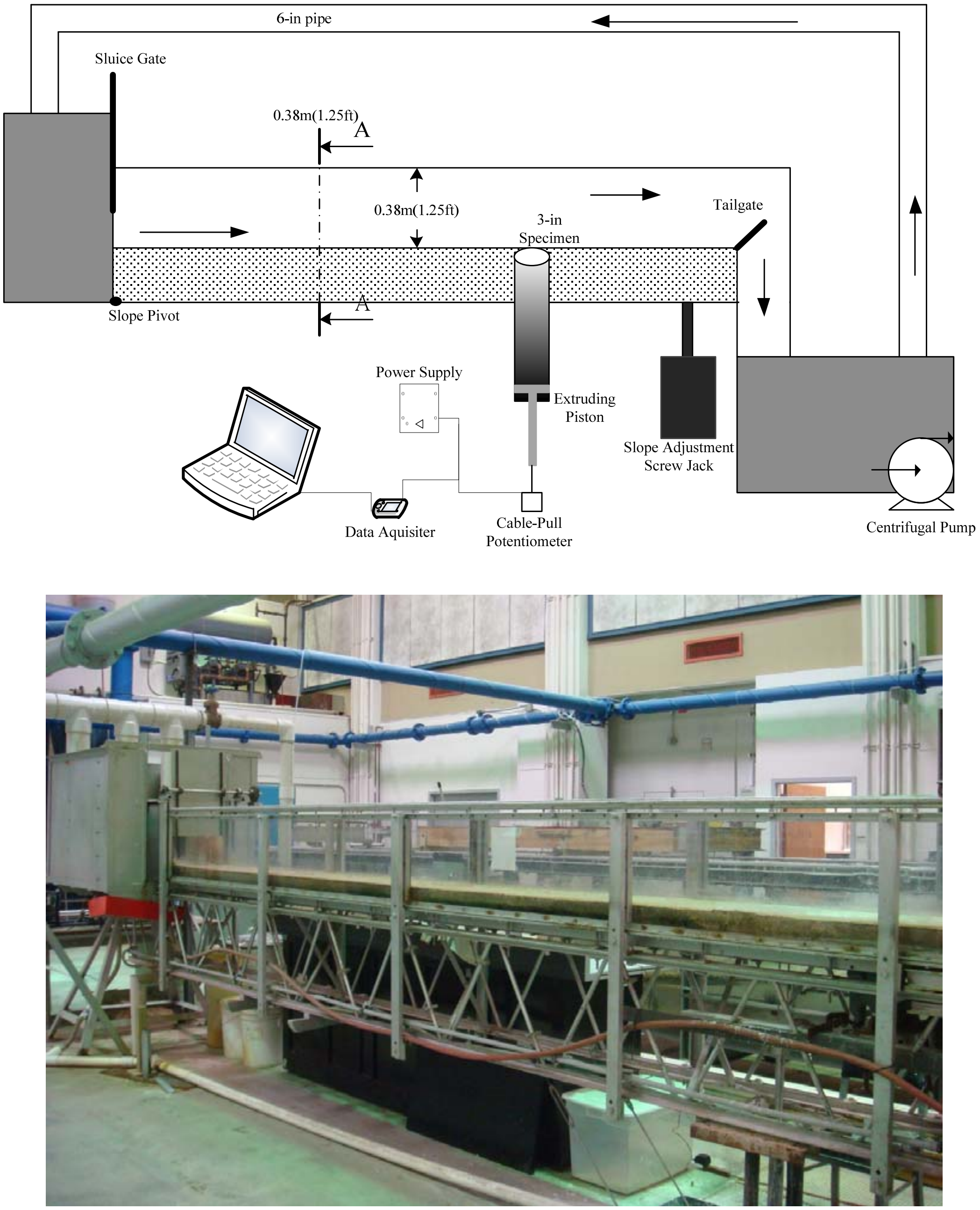

Figure 4.1. Flume apparatus for the erosion test: system layout (upper) and photo (lower).

To begin the flume erosion test of a specimen, the Shelby tube containing the settled sediment mixture was inserted into the flume bottom, and the sediment surface was leveled with the channel bed. Then the top of the specimen was covered by a metal cap as the flow conditions were adjusted to achieve the desired shear stress. Once the test began, the operator gradually extruded the specimen upward with a hydraulic jack to maintain the sediment surface level with its surrounding channel bed as the specimen was eroded. The height of extrusion as a function of time was measured with a cable-pull potentiometer attached to the hydraulic piston that extruded the specimen into the flume. The voltage output from the potentiometer was read through a data acquisition system developed by National Instruments, which was connected to a recording program written with a Matlab interface.

Because the flume experiments relied on visual observation of the sediment surface exposed to the flow, the end of one erosion testing trial was determined by the operator to occur when the eroded sediment in the flow impeded visual observation. Then the specimen surface was covered by the cap, and the flume was entirely shut down, drained, and refilled with fresh water for the next trial. The duration of each test ranged from 30 sec to 10 min, depending on both the erosion resistance of the specimen and the applied bed shear stress. For each test, the depth of the sediment layer in the specimen was recorded, and the water content of a specific sediment depth interval was measured using additional cores that were created and treated identically to the eroded ones. The gravimetric erosion rate (E) per unit surface area was obtained as the product of piston displacement per unit time and sediment dry density, and its minimum value was approximately 0.01 kg/m^2/s.

After a series of erosion tests was conducted under five different applied bed shear stresses (2.15, 2.48, 2.83, 3.24 and 3.49 Pa), the experimental erosion rates were plotted versus the applied bed shear stresses (τ). Then the power law equation for erosion rate, E, given by

$$E = M(\tau - \tau_c)^n \tag{4.1}$$

was used as the model to fit the experimental data points of E vs. τ and obtain the parameters M, n, and τ_c from a nonlinear least-squares optimization technique, the Gauss-Newton algorithm, coded in Matlab. In the Matlab program, parameters M, n, and τ_c were sought iteratively using the Gauss-Newton algorithm such that the model was in best agreement with the input data as determined by the convergence criterion. Graphical fits were made to the data before running the optimization routine to avoid sensitivity to starting parameter values which was less than five percent.

Rheometer Tests

The rheological characteristics of sediment mixtures measured in this study were obtained from yield stress analysis, which was performed with a Haake RheoStress RS75 stress-controlled rheometer (Schramm 1994) since stress-controlled instruments perform well in obtaining yield stress measurements (van Kessel 1998). The rotational rheometer consists of a cup and a concentric cylinder (rotor) which is submerged to rotate in the fluid suspension (see Fig. 4.2). The rotor with the geometry of a cone bottom was chosen to reduce end effects in this study. Under the stress-controlled mode, the rheometer measured the rheological characteristics, such as fluid viscosity as a function of the applied shear stress as an estimate of the strength of cohesive bonds in fine sediments. The rheometer apparatus includes a desktop computer installed with RheoStress monitoring software, the control unit, the cup and rotor sensor, and a constant thermo-controller filled with de-ionized water.

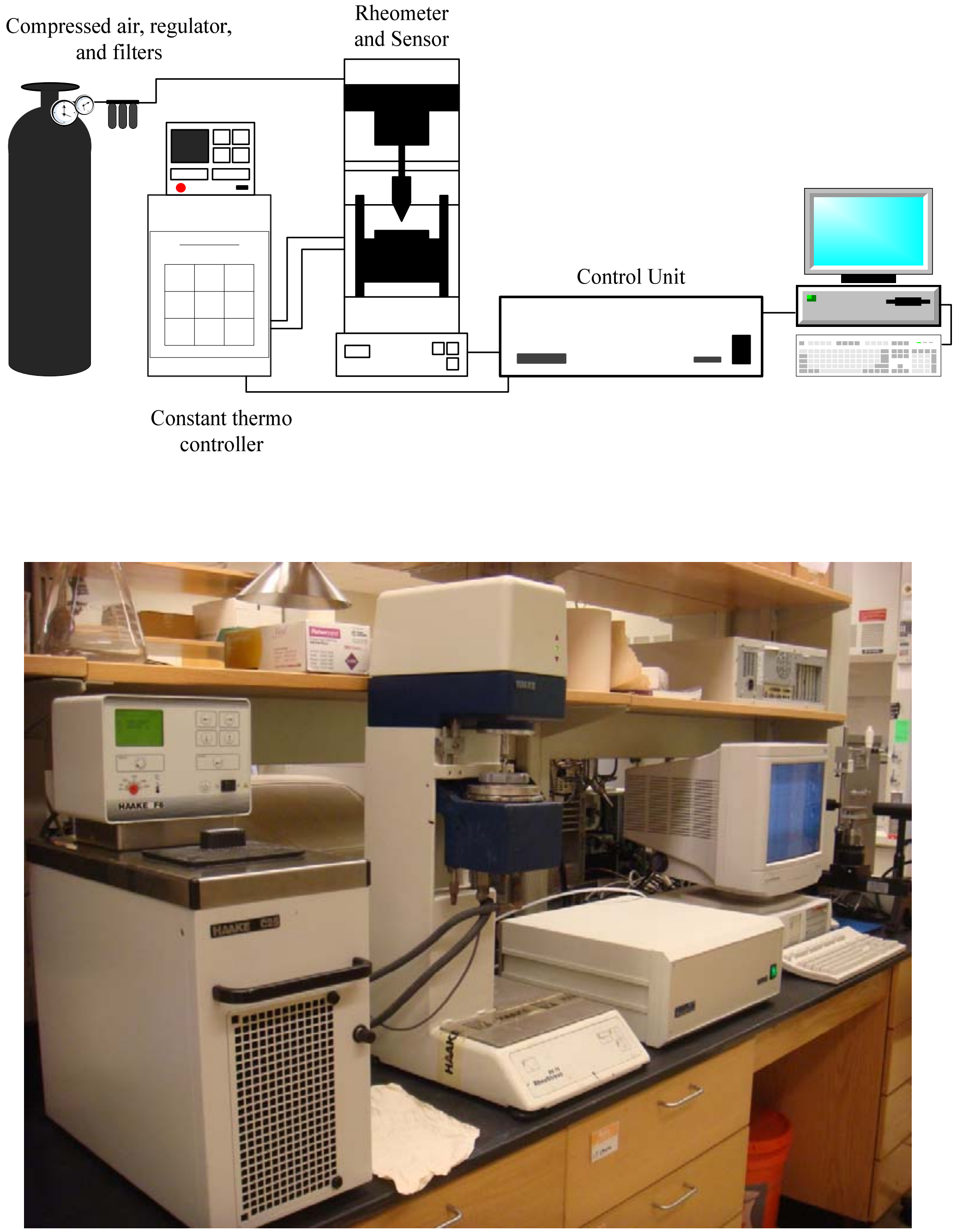

Figure 4.2. Stress-controlled rheometer apparatus: system layout (upper) and photo (lower).

Sediment mixture specimens for the rheometer tests were prepared in an identical manner as those for the flume erosion tests, except that the slurry was poured into the rheometer cup instead of the Shelby tube. After a 24-hour settling period, the excess water was suctioned out and the rheometer test began. Depending on the resistance of the specimen, the apparatus was programmed to logarithmically increase the shear stress from 0.04 Pa to a maximum stress of 12, 24, 48, 96, or 192 Pa over an assigned testing period. For different maximum stress cases, the testing period was determined in each case to produce the same logarithmic rate factor with time (Δ), which is defined as:

$$\Delta = \frac{\log(\tau_{\max} / \tau_{\min})}{t} \tag{4.2}$$

where τ_{max} = the maximum applied shear stress; τ_{min} = 0.04 Pa = the minimum applied shear stress; and t = the testing period. For instance, a 300-second testing period was selected for the case in which applied shear stress increased from 0.04 to 12 Pa, resulting in $\Delta \cong 8.26 \times 10^{-3}$ (s^{-1}) in accordance with previous studies by Hoepner (2001) and Hobson (2008).

In this study, the Herschel-Bulkley model, $\tau = \tau_y + k(\dot{\gamma})^m$ where k and m are experimental constants (Herschel and Bulkley 1926), was selected to estimate τ_y of the sediment specimens by fitting the flow curves from the rheometer tests using the Gauss-Newton algorithm. The yield stress was estimated as the stress value at zero strain rate ($\dot{\gamma}$) for a fitted flow curve. The curve-fitting technique applied the same procedure as that for estimating τ_c. However, measurements of shear stress and strain rate were the input data obtained from rheometer tests, and k, m, and τ_y were the parameters sought to obtain the best-fit model.

EXPERIMENTAL RESULTS

Geotechnical Properties

In Fig. 4.3, the grain size distributions of the sediment mixtures are shown to cover the size range from around one μm to more than 200 μm, which coincides with the grain size range from fine clay (1 to 5 μm) to fine sand (125 to 250 μm) according to the American Geophysical Union

(AGU) scale. However, most of the particles are in the size range of fine clay to very fine sand. The grain size distributions of different sediment layers in the same type of sediment mixture generally show a similar shape and tend to collapse together, except for those of the 10% kaolin specimen. This division in the grain size distribution curves indicates that a significant segregation between sediment layers is observed only in the 10% kaolin specimens due to differential particle settling. Therefore, each layer of the specimens with different kaolin contents was treated as a consistent size mixture rather than a segregated layer except for those of the 10% kaolin specimens.

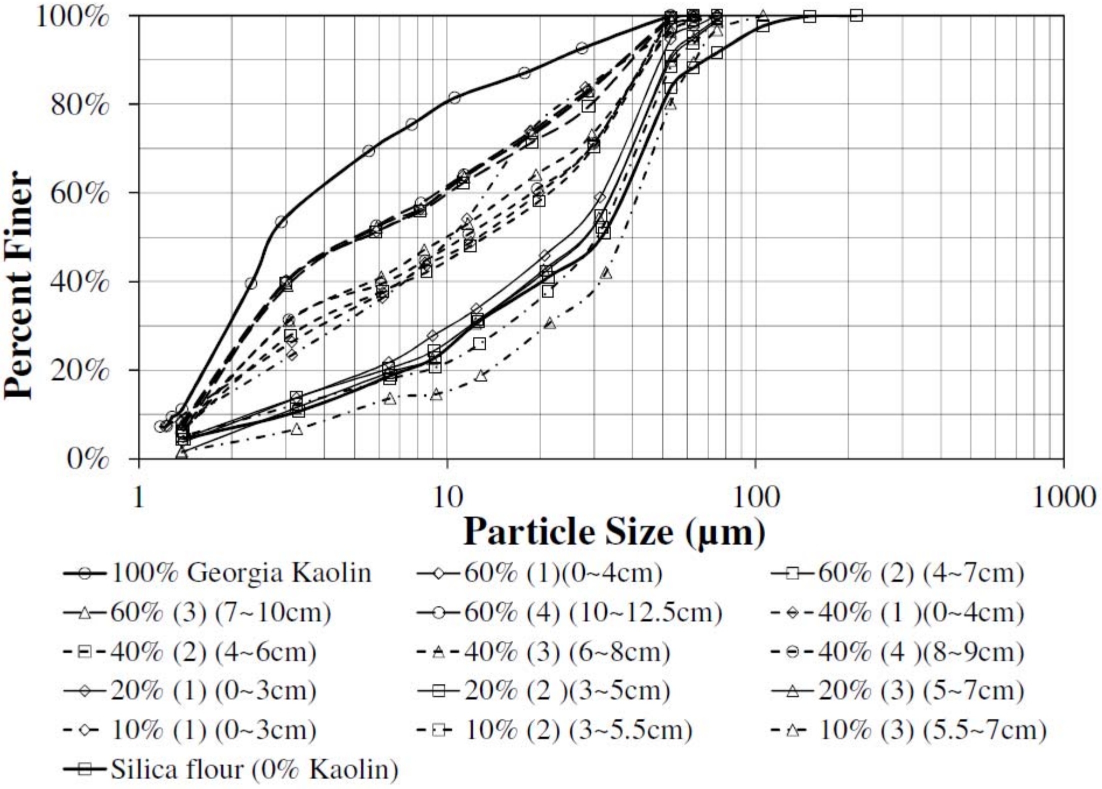

Figure 4.3. Grain size distribution of Kaolinite and silica flour mixtures with percentage Kaolinite specified for each mixture layer number and depth in parentheses (Wang 2013).

For all the specimens, values of the median particle size, d_{50}, varied from 2 to 40 μm, and decreased as the kaolin content increased. Except for the 10% kaolin specimens, sediment layers with the same nominal kaolin content exhibited similar values of d_{50}. The cohesive behavior of the various kaolin-silt mixtures was characterized in terms of the clay-size fraction (*CSF*) of each mixture, defined as the fraction by weight finer than 2 μm, in order to facilitate comparisons with field data and to be consistent with other investigators (e.g. Jacobs et al. 2011). Furthermore, *CSF* is often used to define clay activity in terms of the plasticity index which has been related to critical shear stress in the "soil mechanics" approach (Winterwerp et al. 2012). In this study, *CSF* increased from slightly more than 3% to 30% as the kaolin content in the sediment mixtures increased from 10% to 100%.

As shown in Table 4.2, measurements of water content (w) ranged from 35% to 185%. Except for the 10% kaolin specimens, sediment water content increased with the increase of kaolin content due to the water retention capacity of clay. For most sediment layers, experimental uncertainties led to some scatter in the water content measurements with $CV \cong \pm 5\%$. Bulk density (ρ_b) of the sediment specimens ranged from 1200 kg/m^3 to 1900 kg/m^3. An increasing trend of ρ_b with depth of the sediment layer from the surface was observed; however, scatter in the data and stratification of ρ_b with depth decreased as the kaolin content increased. In particular, sediment specimens made with 100% Georgia kaolin were essentially homogenous with respect to ρ_b throughout the depth of the sediment layers.

Pore Water Chemistry

Temperature measurements of the tap water and sediment mixtures were between 21 and 22°C. The proportion of kaolin in the sediment mixture affected the pH and conductivity values. The tap water used in specimen preparation was neutral (pH value around 7) and had conductivity

Table 4.2. Summary of physical properties, critical shear stress, and yield stress of sediment specimens (Wang 2013).

Specimen type [a]	Mean Water content (%)	Median Partial size (mm)	Mean Bulk density (kg/m^3)	Mean depth interval (mm)	Clay Size Fraction (%)	M values [c]	n values [c]	Critical shear stress (Pa)	Yield stress (Pa)
10% Kaolin (pH~5.9)	74.9	0.010	1552	31.6	13.7	0.0115	3.28	0.490	0.592
	74.2	0.010	1555	25.5	13.7	0.0167	2.83	0.376	0.468
	50.9	0.030	1701	12.7	7.5	0.0141	2.88	0.642	0.446
	40.0	0.030	1799	11.7	3.3	0.0144	2.96	0.812	0.629
	38.3	0.040	1816	11.7	3.3	0.0144	2.96	0.813	0.885
20% Kaolin (pH~5.1)	59.8	0.023	1635	12.4	7.0	0.0234	1.32	0.598	0.525
	53.0	0.026	1682	11.4	7.6	0.0181	1.61	1.157	1.182
	52.9	0.026	1684	10.7	7.6	0.0462	0.851	1.472	0.848
	52.3	0.023	1688	11.4	7.0	0.0181	1.61	1.157	1.184
40% Kaolin (pH~4.8)	85.0	0.013	1502	11.5	14.1	0.0019	2.96	0.841	2.322
	79.0	0.013	1528	10.9	14.1	0.0109	1.57	1.300	2.694
	76.0	0.010	1542	32.9	15.8	0.0025	3.99	1.283	4.086
	74.8	0.012	1548	9.7	15.3	0.0199	1.06	1.583	5.910
	74.4	0.010	1550	9.5	15.8	0.0019	3.04	1.001	4.758
	73.3	0.012	1555	9.7	15.3	0.0199	1.06	1.583	6.268
60% Kaolin (pH~4.7)	97.0	0.006	1456	18.6	20.0	0.0192	0.904	1.347	5.663
	92.6	0.006	1471	18.6	20.3	0.0192	0.904	1.347	6.730
100% Kaolin(1) [b] (pH~4.5)	121.9	0.003	1381	20.1	30.0	0.0334	1.01	0.974	6.247
	121.1	0.003	1383	20.1	30.0	0.0334	1.01	0.974	6.160
100% Kaolin(2) [b]	167.2	0.003	1297	22.2	30.0	0.0268	1.03	1.003	4.375

Note: [a] Only the results of sediments with both critical shear stress and yield stress are listed.

[b] Two different initial water contents were used to prepare 100% kaolin specimens, w=160% for 100% Kaolin(1) and w =100% for 100% Kaolin(2). Only one experimental run was conducted for each layer of 100% Kaolin(1) or (2) under one bed shear stress condition.

[c] The fitting values of experimental coefficients in the power law equation $E = M(\tau - \tau_c)^n$.

values of about 240 μS/cm. However, pH values of the sediment pore water decreased from approximately 6 to 4.5 as the kaolin content increased from 10% to 100% by weight (Table 2).

Ionic strength (*IS*) of pore water in the sediment mixture specimens was estimated from measurements of specific conductivity using the equation proposed by Russell (1976). Values of *IS* of all the sediment mixtures ranged from 2×10^{-3} to 3×10^{-3} M. According to Ravisangar et al. (2005), the pore water *IS* of the sediment mixtures in this study can be classified as a low ionic strength condition (<0.004 M).

Critical Shear stress and Yield stress

The critical shear stress and yield stress, which represent the thresholds of bed shear stress for the erosional and yield strengths of fine sediments, respectively, are two of the most important parameters sought in this study. Experimental values of τ_c and τ_y are given adjacent to the average w and ρ_b of corresponding sediment layers in Table 4.2. Only results for specimens for which both τ_c and τ_y were measured are given in the table. The τ_c values range from 0.3 to 1.6 Pa, and corresponding τ_y values vary from 0.4 to nearly 7 Pa. Values of the fitted parameters M and n from Eq. (4.1) are also given in Table 4.2. Curves with the highest erosion rates correspond with larger values of n which varied from approximately 1 to 4. Critical shear stress tended to increase as n approached the linear case.

Generally, for the specimens with the same kaolin content, both τ_c and τ_y increased as ρ_b increased (and w decreased) corresponding to an increase in depth of sediment layers. For sediment layers having a similar value of ρ_b, higher values of τ_c and τ_y occurred for specimens with higher kaolin contents.

DATA ANALYSIS AND DISCUSSION

In the following section, multiple regression analysis is applied to the critical shear stress data reported herein to relate it to sediment physical properties. The resulting relationship is compared both with the present data and previous laboratory and field data for the purpose of understanding the most important sediment properties affecting erosion thresholds in sediment consisting of a continuous size distribution comprising both fine and coarse grains. Then the yield stress from the rheometer tests is related to the critical shear stress.

Dimensionless Form of Erosional and Yield Strengths

The dimensionless τ_c and τ_y employed by Hobson et al. (2010) are applied in the following analysis and discussion, and they are both of the form of Shields' parameter given by

$$\tau_c^* = \frac{\tau_c}{(\gamma_s - \gamma_w)d_{50}} \tag{4.3}$$

$$\tau_y^* = \frac{\tau_y}{(\gamma_s - \gamma_w)d_{50}} \tag{4.4}$$

where γ_w and γ_s = the specific weight of water and sediment, respectively, and d_{50} = median sediment diameter. The dimensionless form of τ_c is introduced as Shields' parameter τ_c^*, which describes incipient sediment motion in Shields' diagram. Shields' parameter can be interpreted as the ratio of the applied bed shear force initiating sediment motion to the force due to gravity (submerged weight) resisting motion at critical conditions. Similarly, the dimensionless yield stress τ_y^* was considered a useful measure of particle cohesion in the erosion resistance analysis of cohesive sediments by Dade et al. (1992), who investigated the erosion resistance of muds by analyzing the balance of forces acting on cohesive grains at the threshold of motion. In a definition analogous to τ_c^*, the dimensionless variable τ_y^* can be interpreted as the ratio of the interparticle cohesion force at the yield point, as measured by the yield stress, to the submerged weight of particles. Therefore, both τ_c^* and τ_y^* incorporate the gravitational force as a reference force.

Multiple Regression Analysis

To investigate the relationships among the physical properties and erosional strengths of sediments measured in this study, multiple regression analysis was applied. From previous studies (e.g. Grabowski et al. 2011; Hobson 2008; Ravisangar et al. 2005), some of the geotechnical characteristics of sediments are considered as possible predictors in a multiple regression analysis to estimate the response variables of interest in this study The geotechnical characteristics include water content (*w*) as a decimal fraction; clay-size fraction (*CSF*) defined as the decimal fraction of particles smaller than 2 μm by weight; bulk density (ρ_b) defined as the mass of water plus sediment divided by the total volume; and median particle size (d_{50}) as expressed in its dimensionless form in one version of Shields' diagram (Sturm 2009):

$$d_* = \left[\frac{(SG-1)gd_{50}^3}{\nu^2} \right]^{1/3} \tag{4.5}$$

in which SG = specific gravity of the sediment, and ν = kinematic viscosity of water.

The regression model for predicting τ_c^* was constructed by the following procedure. First, possible predictors were initially formed by utilizing all of them in stepwise regression and then forming subsets by removing predictors one at a time. The most influential predictors were identified based on the Aikake's information criterion (AIC_p) which balances the number of predictors against the goodness of fit to avoid over-fitting. Secondly, the value of Mallow's C_p for the model with a subset of the selected predictors was compared to that for the full model, which consisted of all possible predictors, for validation. In using the C_p criterion, subsets of predictors were sought for which C_p was small and close to p, the number of predictors. Moreover, the dependency among the selected predictors was investigated to determine if an interaction effect may be present by plotting the response variable, y, fitted without the interaction term (x_1x_2), against x_1x_2 (Kutner et al. 2004).

The final regression model was selected based on the minimum value of the standard error of estimate (*S.E.E.*) of the regression given by

$$S.E.E. = \sqrt{\frac{\sum_{i=1}^{n}(y_i - \hat{y}_i)^2}{n-p}} \tag{4.6}$$

in which n = the number of measurements, p = the number of parameters in the regression model, y_i = the i^{th} measured value of the response variable and $\hat{y}_i$ = the corresponding predicted value (Kutner et al. 2004).

Regression Model for Shields' Parameter τ_c^*

From the stepwise multiple regression analysis just described, the model determined to best predict Shields' parameter for the silt-clay mixtures in this study is given as:

$$\hat{\tau}_c^* = 8.46 - 27.76\,w + 73.69\,CSF + 83.22\,(w \times CSF) \tag{4.7}$$

The selected independent variables expressed as decimal fractions include *w*, *CSF*, and the interaction term, $w \times CSF$. The coefficients in Eq. (4.7) are statistically significant at the level of $P<0.001$. The statistics relating to the goodness-of-fit of this model are: $R^2 = 0.88$, ${R_a}^2 = 0.88$, and $S.E.E._{\tau_c^*} = \pm 3.17$ in which R^2 = coefficient of determination; R_a^2 = adjusted coefficient of determination to account for the number of predictors; and $S.E.E._{\tau_c^*}$ = the standard error of estimate in τ_c^* of the best-fit equation. A negative and a positive effect of *w* and *CSF*, respectively, on Shields' parameter are indicated by the coefficients with opposite signs on these two terms in Eq. (4.7). This finding is confirmed by the studies of Bale et al. (2006), Amos et al. (2004), and Watts et al. (2003) who concluded that the erosion resistance of fine-grained sediments increases as w decreases but as CSF increases. Additionally, in sediment composed of predominantly fine-grained particles, a decrease of w often leads to an increase in ρ_b and thus results in a higher erosion resistance (Grabowski et al. 2011; Debnath et al. 2007).

Although w and CSF have opposite effects on τ_c^*, the positive sign of the interaction term ($w \times CSF$) plays an important role in the final relationship. It is likely a result of the positive correlation between w and CSF found in this study and the literature (e.g. Gerbersdorf et al. 2007; Amos et al. 2004; Watts et al. 2003), and it acts to significantly reduce the rate of decrease of τ_c^* with w at high values of CSF as shown in Fig. 4.4. At low values of CSF, the interaction term is of the same order as the CSF term and taken together they result in higher rates of decrease of τ_c^* with w than for larger CSF values.

In Fig. 4.4, the τ_c^* measurements for silt-clay mixtures in this study are compared with the best-fit curves of Eq. (4.7) for specified CSF values as a parameter. Because the maximum w is subject to the value of CSF, the data points which plot in the upper right quadrant of Fig. 4.4 for high values of w belong to the sediments with higher CSF. The best-fit curves for sediment mixtures with 30%-CSF compare well with the corresponding data points. For sediment mixtures with high CSF, τ_c^* is only weakly influenced by changes in w and thus is expected to be dominated by interparticle forces of the clay. For intermediate values of water content and CSF, the rate of decrease of τ_c^* with increasing water content becomes less for larger values of CSF as it overcomes the influence of water on the particle interaction. For small values of both CSF

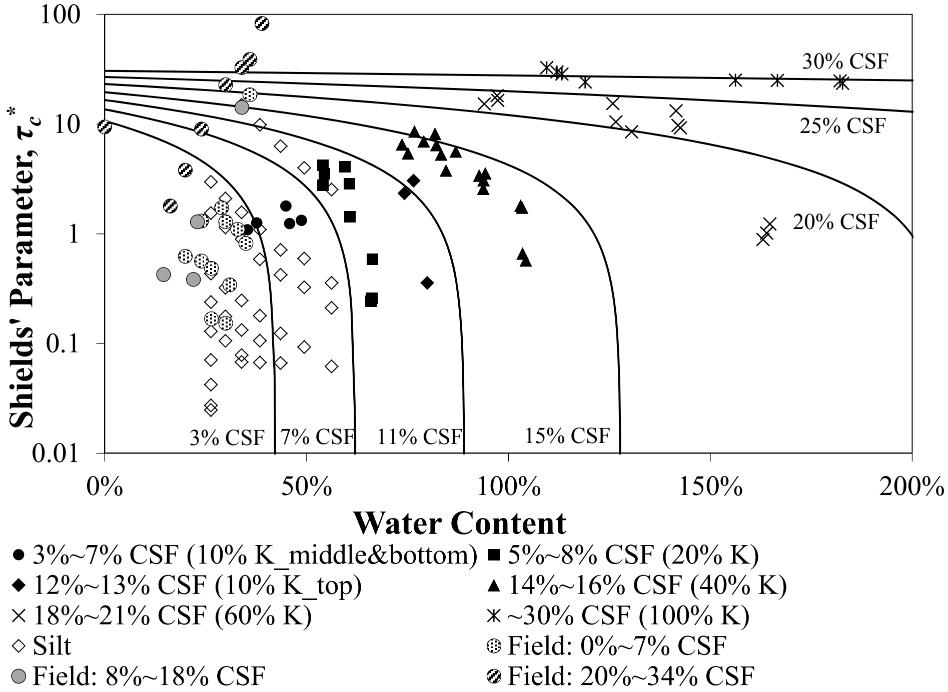

Figure 4.4. Best-fit relationship for Shields' parameter as a function of water content and *CSF* for kaolin-silica flour mixtures shown as solid curves compared with data from this study, field data from Navarro (2004) and Hobson (2008), and laboratory silt data from Roberts (1998). (Wang 2013).

(3%-7%) and *w*, the kaolin-silt mixture data points for τ_c^* are nearly horizontal indicating a weak influence of water content and perhaps a transition in cohesive behavior consistent with the work of van Ledden et al. (2004) who showed that the structural framework of sand-mud mixtures changes at around 5% to 10% *CSF*. However, the present data contain no sand, and van Ledden et al. acknowledge that the transition may also depend on water content.

Values of τ_c^* for laboratory data measured by Roberts et al. (1998) are also shown in Fig. 4.4 in which the logarithmic vertical scale shows the wide range in magnitudes of τ_c^* for both laboratory and field data. These data represent quartz particles having different d_{50} but prepared with the same pre-determined *w,* or bulk density. Depending on the grain size distributions, the *CSF* ranged from 0% to 6% of the specimens although the sediments were composed of quartz particles alone. In Fig. 4.4, more than 85% of the Roberts et al. (1998) data fall below and to the left of the 7%-*CSF* curve from Eq. (4.7). Their data show an increase in τ_c^* for a given bulk density (water content) corresponding to a decrease in d_* consistent with trends in Shields' diagram for silt particles, which is an alternative method of presenting their results with bulk density (or water content) as a second independent variable. However, despite the trend in their data of increasing τ_c^* with decreasing d_*, the data points fall above Shields' relationship for silt by varying amounts as a function of bulk density. Grabowski et al. (2011) suggested the apparent silt particle cohesion might be due to biofilms and/or biological growth on the silt particles because of the long consolidation times. In any case, their data plot in the same region as data from the current study showing weaker cohesive behavior for smaller values of *CSF*.

While Eq. (4.7) was constructed based on the silt-clay mixtures used in this study and thus was meant to predict τ_c^* of sediments composed of predominantly fine-grained particles, it is also compared in Fig. 4.4 with measured values of τ_c^* for river bed sediments collected in the field at bridge sites throughout Georgia by Shelby tube sampling. The sampling sites included the physiographic regions of the Piedmont and Coastal Plain. The field samples were tested in the same erosion flume as used in the present study (Hobson et al. 2010). Seventy five percent of the field data points plotting below the *CSF* = 7% best-fit curve (Eq. (4.7)) have *CSF* proportions from 0% to 7% in Fig. 4.4 and have water contents less than about 40%. In addition, an increasing trend of τ_c^* with *CSF* is observed among the field data for $\tau_c^* \geq 1$ in agreement with values from the best-fit curves and the laboratory data from this study which tends to confirm the choice of *CSF* as an independent variable. If a new regression analysis is applied to the combined data set consisting of sediment mixtures in this study, the field data from Georgia, and the laboratory data of Roberts et al. (1998) shown in Fig. 4.4, the best-fit relationship has very similar coefficients to those of Eq. (4.7) (<18% difference) but R^2 drops from 0.88 to 0.57. Correspondingly, a comparison of Eq. (4.7) with all of the data shows a similar drop in predictive power. In other words, Eq. (4.7) is consistent with the field data, but it loses some of its predictive capability when including the coarser sediments in the combined data set. The field data include d_{50} values that vary from approximately 0.01 to 1.0 mm with a mean value of 0.27 mm so they are generally more heterogeneous and coarser than the sediment mixtures in the present study (d_{50} = 0.002 to 0.04 mm), but they do have an overlapping size range. In addition, they may include different types of clay although kaolinite is prevalent in Georgia sediments (Bates 1963). Hobson et al. (2010) showed that τ_c^* for the field data is more closely related to d_* and percent fines (silt + clay); that is, in Shields' diagram of τ_c^* vs. d_* with percent fines as the second independent variable.

Relationship between Erosional and Yield Strengths

In a research study of mud erosion resistance, Williams and Williams (1989) related τ_y and τ_c through a systematic analysis of fine sediment properties. They proposed a potential scaling for τ_c, which is given by Dade et al. (1992):

$$\tau_L \leq \tau_c \leq \tau_y \tag{4.8}$$

where τ_L = the upper limit of shear stress under which fine sediments show linear viscoelastic behavior. Therefore, a shear stress having a magnitude between τ_L and τ_y results in a nonlinear viscoelastic deformation because of an incipient breakdown of some weak interparticle bonds. As a result, this intermediate stress value can be considered as the threshold of bed shear stress at which particle/aggregate movement is initiated, i.e. τ_c. When the stress exceeds τ_y, the breakage of most interparticle bonds leads to an irreversible flow deformation such that τ_y can be considered an upper bound of τ_c.

Empirical correlations of τ_y and τ_c have been suggested by previous researchers such as Migniot (1968) and Otsubo and Muraoka (1988). In particular, Migniot (1968) proposed two relationships corresponding to high and low yield strength natural muds, respectively. The high yield strength muds were cohesive sediments with $\tau_y > 1.6$ Pa and the low yield strength muds had values of $\tau_y < 1.6$ Pa. In their research, τ_c was proportional to the square root of τ_y for low yield strength or weakly cohesive muds and increased linearly with τ_y for high yield strength muds.

Based on general correlations found in the literature between τ_c and τ_y, a relationship was sought between Shields' parameter and the dimensionless yield stress data measured for all the sediment mixtures in this study as shown in Fig. 4.5. The best-fit relationship from regression analysis is given by

$$\hat{\tau}_c^* = 1.42\left(\tau_y^*\right)^{0.55} \tag{4.9}$$

for which the standard error of estimate in τ_c is ±0.22 Pa and $R^2 = 0.96$. There is some agreement between Eq. (4.9) and Migniot's proposed square-root power on yield stress for low yield strength muds, but here it is extended over the full range of data in this study. Although τ_y^* reflects the breaking of many interparticle bonds to the point of irreversible flow deformation as in mass erosion, and τ_c^* tends to represent the beginning of that process, both are influenced similarly by w and *CSF*. It can be observed from Fig. 4.5 that τ_c^* and τ_y^* are of the same order for τ_y^* less than about two, and then τ_y^* increases much more rapidly than τ_c^* for larger values. In the flume, surface erosion of flocs was observed at lower shear stresses. Larger aggregates were eroded from the surface at the highest value of shear stress, although mass failure of the entire bed did not occur. Thus, the observation that τ_c^* and τ_y^* are of similar magnitude in the lower

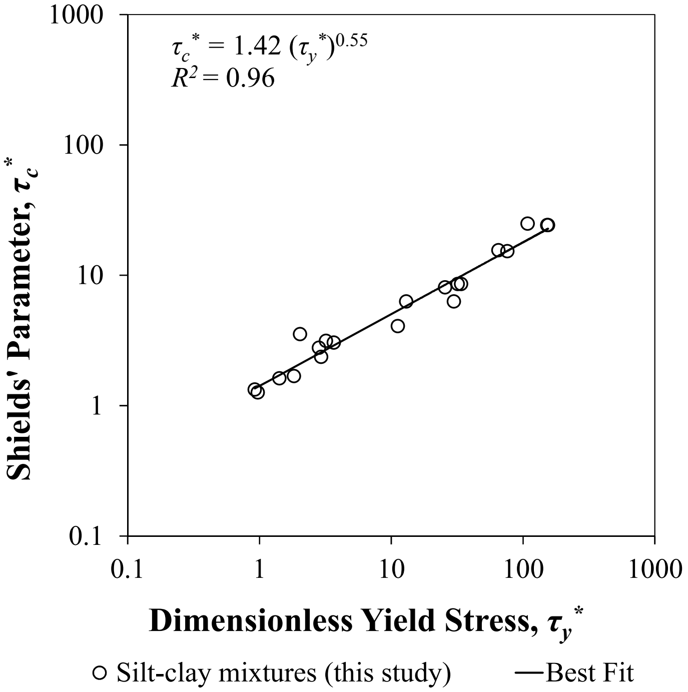

Figure 4.5. Correlation of Shields' parameter with dimensionless yield stress (Wang 2013).

range of Fig. 4.5, where cohesive forces are weaker, may be indicative of an approach to mass erosion in the flume for these cases. The best-fit equation between τ_c^* and τ_y^* is necessarily specific to kaolinite *CSF*, but it is significant that a direct relationship between the erosional and yield strengths exists which unifies erosion data for both high and low yield strength sediment mixtures of clay and silt.

SUMMARY

In this study, silt-clay sediment mixtures with different kaolinite contents, ranging from 10% to 100%, were prepared by mixing ground silica and Georgia kaolinite with water for the purpose of measuring their erosion resistance and relating it to sediment properties. Geotechnical tests were carried out to obtain the physical properties of the specimens including water content, bulk density, and grain size distribution. The temperature, pH value, and specific conductivity of the sediment mixtures were measured by a portable pH/conductivity meter. The critical shear stress and yield stress of the sediment mixtures were determined through hydraulic flume experiments and rheometer tests, respectively.

From the laboratory work and data analysis, relationships among the critical shear stress, yield stress, and the sediment physical properties were developed from multiple regression analysis. In dimensionless form, a nonlinear relationship for Shields' parameter as a function of w and CSF is proposed. The measured flume and rheometer data for Shields' parameter (τ_c^*) and the dimensionless yield stress (τ_y^*) show that a unique relationship exists between the two measures of erodibility that could be exploited with rheometer tests of bridge sediment samples.

LIST OF SYMBOLS

AIC_p = Akaike's information criterion for subset selection;

CSF = clay-sized fraction expressed as decimal fraction of particles smaller than 2 μm by mass;

C_p = Mallows' C_p criterion for regression subset selection;

CV = coefficient of variation;

d = sediment grain size;

d_{50} = median particle size;

E = gravimetric erosion rate of sediments;

$Fines$ = fine content; decimal fraction of particles smaller than 62 μm by mass;

IS = ionic strength;

k_s = equivalent sand-grain roughness height;

k, m = constants in Herschel-Bulkley equation;

M, n = constants in the power-law equation of sediment erosion;

R^2 = coefficient of determination;

R_a^2 = adjusted coefficient of determination;

SE = standard error in repeated measurements;

$S.E.E.$ = standard error of estimate of best-fit relationship;

SS_E = unexplained variance (random variance) of the response variable;

T = temperature;

t = time;

u_* = shear velocity;

w = water (moisture) content;

x_k = k^{th} predicting variable;

y_i = i^{th} data point of the response variable;

$\dot{\gamma}$ = shear strain rate;

γ_w = specific weight of water;

γ_s = specific weight of sediments;

Δ = rheometer strain rate increment per unit time;

μ_j = mean of variable *j;*

ν = kinetic viscosity of water;

ρ_b = bulk density of sediments;

σ_j = standard deviation of variable *j;*

τ = flume bed shear stress or applied rheometer shear stress;

τ_c = critical shear stress;

τ_c^* = Shields' parameter;

τ_L = upper limit of shear stress for materials showing linear viscoelastic behavior;

$\tau_{\min}$, $\tau_{\max}$ = minimum and maximum applied shear stress during rheometer tests;

τ_y = Herschel-Bulkley yield stress;

τ_y^* = dimensionless yield stress.

REFERENCES

Amos, C. L., Bergamasco, A., Umgiesser, G., Cappucci, S., Cloutier, D., DeNat, L., Flindt, M., Bonardi, M., and Cristante, S. (2004). "The stability of tidal flats in Venice lagoon--the results of in-situ measurements using two benthic, annular flumes." *J. Marine Syst.*, 51(1-4), 211-241.

ASTM C136 (2001). "Standard test method for sieve analysis of fine and coarse aggregate." American Society for Testing and Materials,West Conshohochen, PA.

ASTM D 1140 (2000). "Standard test methods for amount of material in soils finer than the No. 200 (75-μm) sieve." American Society for Testing and Materials, West Conshohochen, PA.

ASTM D 2216 (2005). "Moisture content of soil." American Society for Testing and Materials, West Conshohochen, PA.

ASTM D422-63 (2002). "Standard test method for particle-size analysis of solids." American Society for Testing and Materials, West Conshohochen, PA.

ASTM D4318-10 (2010). “Standard test methods for liquid limit, plastic limit, and plasticity index of soils.” American Society for Testing and Materials, West Conshohocken, PA.

Bale, A. J., Widdows, J., Harris, C. B., and Stephens, J. A. (2006). "Measurements of the critical erosion threshold of surface sediments along the Tamar Estuary using a mini-annular flume." *Cont. Shelf Res.*, 26(10), 1206-1216.

Bates, T. F. (1963). “Geology and mineralogy of the sedimentary kaolins of the southeastern United States-A review.” *Clays and Clay Minerals*, 12: 177-194.

Dade, W. B., Nowell, A. R. M., and Jumars, P. A. (1992). "Predicting erosion resistance of muds." *Mar. Geol.*, 105(1-4), 285-297.

Debnath, K., Nikora, V., Aberle, J., Westrich, B., and Muste, M. (2007). "Erosion of cohesive sediments: Resuspension, bed load, and erosion patterns from field experiments." *J. Hydraul. Eng.*, 133(5), 508-520.

Gerbersdorf, S., Jancke, T., and Westrich, B. (2007). "Sediment properties for assessing the erosion risk of contaminated riverine sites: An approach to evaluate sediment properties and their covariance patterns over depth in relation to erosion resistance. First investigations in natural sediments." *J. Soil. Sediment.*, 7(1), 25-35.

Grabowski, R. C., Droppo, I. G., and Wharton, G. (2011). "Erodibility of cohesive sediment: The importance of sediment properties." *Earth-Sci. Rev.*, 105(3-4), 101-120.

Herschel, W. H., and Bulkley, R. (1926). "Measurement of consistency as applied to rubber benzene solutions." *Proceedings of American Society for Testing Materials*, 26, 621-633.

Hobson, P. M. (2008). "Rheologic and flume erosion characteristics of Georgia sediments from bridge foundations." M.S. Thesis, Georgia Institute of Technology, Atlanta, GA.

Hobson, P., Navarro, R., and Sturm, T.W. (2010). "Erodibility of sediment at bridge foundations in Georgia." *Proceedings of the 2nd Joint Federal Interagency Conference (9th Federal Interagency Sedimentation Conference and 4th Federal Interagency Hydrologic Modeling Conference)*, June 27-July 1, Las Vegas, Nevada, CD-ROM ISBN 978-0-9779007-3-2, (http://acwi.gov/sos/pubs/2ndJFIC/index.html).

Hoepner, M. A. (2001). "Stability of cohesive sediments from flume and rheometer measurements." M.S. Thesis, Georgia Institute of Technology, Atlanta, GA.

Jacobs, W., Le Hir, P., Van Kesteren, W., and Cann, P. (2011). "Erosion threshold of sand-mud mixtures." *Continental Shelf Research*, 31, S14-S25.

Karmaker, T., and Dutta, S. (2011). "Erodibility of fine soil from the composite river bank of Brahmaputra in India." *Hydrol. Process.*, 25(1), 104-111.

Kutner, M., Nachtsheim, C., Neter, J., and Li, W. (2004). *Applied linear statistical models*, 5th ed., McGraw-Hill, New York.

Lee, SeungOh and Sturm, T. W. (2009),” Effect of sediment size scaling on physical modeling of bridge pier scour.” *J. Hydraul. Eng.*, 135(10), 793-802.

Mehta, A. J. and W. H. McAnally (2008). "ASCE Sedimentation Engineering (Chapter 4)." Manual 110 2, 253-305.

Migniot, C. (1968). "Etude des propriétés physiques de différents sédiments très fins et de leur comportement sous des actions hydrodynamiques." *La Houille Blanche*, 7, 591-620.

Mitchener, H., and Torfs, H. (1996). "Erosion of mud/sand mixtures." *Coast. Eng.*, 29(1-2), 1-25.

Navarro, H. R. (2004). "Flume measurements of erosion characteristics of soils at bridge foundations in Georgia." M.S. Thesis, Georgia Institute of Technology, Atlanta, GA.

Nguyen, Q. D., and Boger, D. V. (1992). "Measuring the flow properties of yield stress fluids." *Annu. Rev. Fluid Mech.*, 24(1), 47-88.

Osman, A. M., and Thorne, C. R. (1988). "Riverbank stability analysis: I. Theory." *J. Hydraul. Eng.*, 114(2), 134-150.

Otsubo, K., and Muraoka, K. (1988). "Critical shear stress of cohesive bottom sediments." *J. Hydraul. Eng.*, 114(10), 1241-1256.

Ravisangar, V., Dennett, K. E., Sturm, T. W., and Amirtharajah, A. (2001). "Effect of sediment pH on resuspension of kaolinite sediments." *J. Environ. Eng.*, 127(6), 531-538.

Ravisangar, V., Sturm, T. W., and Amirtharajah, A. (2005). "Influence of sediment structure on erosional strength and density of kaolinite sediment beds." *J. Hydraul. Eng.*, 131(5), 356-365.

Reddi, L. N., and Bonala, M. V. S. (1997). "Critical shear stress and its relationship with cohesion for sand-kaolinite mixtures." *Can. Geotech. J.*, 34(1), 26-33.

Roberts, J., Jepsen, R., Gotthard, D., and Lick, W. (1998). "Effects of particle size and bulk density on erosion of quartz particles." *J. Hydraul. Eng.*, 124(12), 1261-1267.

Russell, L. L. (1976). "Chemical aspects of groundwater recharge with wastewaters," Ph.D. Thesis, University of California at Berkeley, Berkeley.

Santamarina, J. C. (2001). "Soil behavior at the microscale: Particle forces. *Proc. Symposium on soil behavior and soft ground construction*, *in honor of Charles C. Ladd*.", MIT, Cambridge, 1-32.

Santamarina, J. C., Klein, K. A., Wang, Y. H., and Prencke, E. (2002). "Specific surface: determination and relevance." *Can. Geotech. J.*, 39(1), 233-241.

Schramm, G. (1994). *A practical approach to rheology and rheometry*, HAAKE, Karlsruhe, Germany.

Sturm, T.W. (2009). “*Open channel hydraulics*.” 2nd edition, McGraw-Hill, New York.

Sturm, T. W. (2006). “Scour around bankline and setback abutments in compound channels.” *J. Hydraul. Eng*., 132(1), 21-32.

Ternat, F., Boyer, P., Anselmet, F., and Amielh, M. (2008). "Erosion threshold of saturated natural cohesive sediments: Modeling and experiments." *Water Resour. Res.*, 44(11), W11434.

van Kessel, T. (1998). "Rheology of cohesive sediments: Comparison between a natural and an artificial mud." *J. Hydraul. Res.*, 36(4), 591-612.

van Ledden, M., van Kesteren, W. G. M., and Winterwerp, J. C. (2004). "A conceptual framework for the erosion behaviour of sand-mud mixtures." *Cont. Shelf Res.*, 24(1), 1-11.

Wang, Y.-C. (2013). "Effects of physical properties and rheological characteristics on critical shear stress of fine sediments," Ph.D. Thesis, Georgia Institute of Technology, Atlanta.

Watts, C. W., Tolhurst, T. J., Black, K. S., and Whitmore, A. P. (2003). "In situ measurements of erosion shear stress and geotechnical shear strength of the intertidal sediments of the experimental managed realignment scheme at Tollesbury, Essex, UK." *Estuar. Coast. Shelf Sci.*, 58(3), 611-620.

Williams, P. R., and Williams, D. J. A. (1989). "Rheometry for concentrated cohesive suspensions." *J. Coastal Res.*, Spec. Iss.5, 151-164.

Williamson, H., and Ockenden, M. (1996). "Isis: An instrument for measuring erosion shear stress in situ." *Estuar. Coast. Shelf Sci.*, 42(1), 1-18.

Winterwerp, J. C., W. G. M. van Kesteren, B. van Prooijen and W. Jacobs (2012). "A conceptual framework for shear flow induced erosion of soft cohesive sediment beds." *J. Geophys. Res.*, 117, C10020, 17.

CHAPTER 5

SUMMARY AND CONCLUSIONS

SUMMARY

During extreme hydrologic events, bridges may be subjected to submerged orifice flow and overtopping because they were not designed for such large flows. As a result, such bridges are vulnerable to excessive scour of the foundations and possible failure. In this research, both the hydrodynamics of the flow and the scour resistance of fine sediments were studied to improve prediction of scour depths under extreme flooding conditions. The research proceeded on three related fronts and the results are described in Chapters 2, 3, and 4. First, experimental measurement of the scour depth and flow field in a large compound channel flume was undertaken to develop a predictive relationship for combined abutment/contraction scour. These experiments included a realistic river cross section and bridge geometry with erodible embankments as well as river bed. Second, a state-of- the- art computational fluid dynamics model was applied to a bridge overtopping flow to predict the turbulence properties of the flow field thought to drive the physical scour process. The numerical model utilized large-eddy simulation and was enhanced with an accurate algorithm for predicting the water surface profile through the bridge which is essential for obtaining realistic estimates of turbulent flow properties. Finally, laboratory mixtures of fine sediments were tested in an erosion flume to develop a relationship for critical shear stress at the threshold of scour. In addition, the critical shear stress was related to the sediment yield stress measured in a rheometer. While most previous research efforts aimed at the bridge scour problem have focused on one single aspect or another, this research is unique in the fact that it incorporates a comprehensive approach that recognizes not only the importance of predicting the hydrodynamic properties of the flow field, including turbulence, that are responsible for producing scour, but also the resisting forces of sediment erosional strength, especially in the particular case of fine sediments which experience cohesive, interparticle forces.

CONCLUSIONS

The following conclusions are drawn from this research:

- Abutment and lateral contraction clear-water scour can be treated as a single process and predicted as an amplification factor times the theoretical long contraction scour as a reference variable.
- Scour due to submerged orifice and overtopping flows can be predicted with the same relationship for amplification factor.
- A separate amplification factor is required for short-setback abutments (SSA) and bankline abutments (BLA) vs. long setback abutments (LSA). The criterion for these two categories is that $W/y_{f1} > 6$ for LSA, where W is the distance from the toe of the face of the abutment to the bank of the main channel and y_{f1} is the approach flow depth in the floodplain.
- The amplification factor depends on the turbulent kinetic energy generated by flow separation as the flow comes around the abutment and is constricted in the bridge section.
- The amplification factor can also be approximated by the ratio of discharge per unit width in the bridge section to that in the approach flow.
- The CFD results provide a window into the complex turbulent processes involved in bridge overtopping. In addition to the horizontal flow separation vortices around the abutment, a substantial helical arch vortex spans over the bridge.

- Bridge overtopping creates a horizontal recirculation zone downstream of the abutment and flow contraction underneath the deck as shown by the CFD results. The overtopping flow reaches critical conditions on the deck and creates areas of very high turbulence as it plunges in the form of an undular hydraulic jump downstream of the bridge.
- The area where horizontal and vertical recirculation zones meet is characterized by high magnitudes of turbulent kinetic energy, TKE, and formation of substantial shear layers that are easily seen in the CFD results.
- The location of highest bed-shear stress, i.e. underneath the deck where the flow is contracted and accelerated, does not correspond to the location of maximum TKE based on the CFD results.
- The dimensionless critical shear stress (Shields' parameter) of fine sediment mixtures of kaolinite and silt tested in the erosion flume increases with increasing *CSF* and decreasing water content.
- The best-fit equation developed for Shields' parameter from laboratory data is consistent with field data collected in Georgia for fine-grained sediments, although the field sediments were somewhat coarser and more poorly-sorted mixtures.
- Sediment yield stress obtained from rheometer tests is a surrogate measure of critical shear stress for erosion. A strong relationship exists between the two variables that could be used to advantage in simpler rheometer tests in comparison to flume tests.
- The critical shear stress and yield stress relationships derived in this research are necessarily limited to kaolinite clays and to mixtures of kaolinite and silt having (1) ρ_b = 1200 to1900 kg/m^3; (2) w = 35 to 185%; (3) d_{50} in the range of silt-size particles from 0.002 to 0.04 mm; and (4) pore water of low *IS* and pH values from 4 to approximately 6.

- More experiments are needed to establish fundamental connections between sediment particle structure and physical sediment properties, but the methodology developed herein can be applied to hydraulic engineering situations in which erosion resistance is an important parameter.

Taken together as a comprehensive approach, the results of this research provide a road map to future bridge scour research that incorporates and combines the results of realistic laboratory experiments, sophisticated numerical modeling and the essential characterization of sediment erodibility.